nature immunology

Article

https://doi.org/10.1038/s41590-025-02232-5

LARP4-mediated hypertranslation drives T cell dysfunction in tumors

Received: 8 January 2025

Accepted: 17 June 2025

Published online: 22 July 2025

Check for updates

Yi Liu[1,2,13], Haochen Ni[3,4,5,13], Jie Li[3,4,13], Jing Yang[3,4,5], Ivann Sekielyk[2,6], Bryan E. Snow[2], Zihao Zhang[1,7,8,9], Feifan Zhang[3,4,5], Michael St. Paul[2], Jinyi Han[1,7,8,9], Meghan Kates[2,10], Shaofeng Liu[2], Yawei Zhang[3,4], Zurui Huang[3,4,5], Yin Xu[3,4,5], Samuel D. Saibil[2,10], Tak W. Mak[2,10,11,12], Dali Han[3,4,5] ✉ & Meng Michelle Xu[1,7,8,9] ✉

Adoptive T cell therapies have therapeutic potential for treating solid tumors, but long-term efficacy is limited by reduced functional fitness and poor persistence within the tumor microenvironment. Here we show that intratumoral T cells undergo translatome remodeling, transitioning into a hypertranslational state as they acquire dysfunctional traits. The RNA-binding protein LARP4 is a translation regulator that drives hypertranslation and dysfunction by selectively enhancing the translation of nuclear-encoded oxidative phosphorylation (OXPHOS) mRNAs in exhausted T cells, disrupting OXPHOS subunit balance and causing mitochondrial dysfunction. Knockout of *Larp4* in tumor-specific $CD8^+$ T cells reduces hypertranslation, restores mitochondrial function, mitigates exhaustion and enhances effector persistence, resulting in enhanced anti-tumor responses. Additionally, *LARP4* knockdown in chimeric antigen receptor T cells prevents terminal exhaustion and improves the response to liquid and solid tumors. This study highlights translation dysregulation as a determinant of T cell dysfunction in tumors.

Adoptive T cell therapies have shown promising results in the treatment of liquid tumors but limited efficacy against solid tumors, primarily because of reduced fitness and insufficient persistence of effector T cells (T_{EFF})[1,2]. T cells within the tumor microenvironment (TME), faced with chronic antigen exposure and metabolic stress, gradually lose their effector capabilities and transition into a dysfunctional state (also known as exhaustion)[3], characterized by impaired cytokine production, decreased cytotoxic activity, reduced proliferative capacity and metabolic dysfunction[4]. Improving T cell outcomes requires strategies promoting long-lasting functional T cells ('effector persistence') over 'exhaustion persistence'[5,6]. One key factor in the persistence of anti-tumor responses is the presence of stem-like progenitor exhausted T cells (T_{PEX}), expressing TCF1, TOX and Ly108, which originate in the tumor-draining lymph nodes (TdLNs) and exhibit self-renewal and differentiation plasticity[6,7]. Within the TME, chronic antigen stimulation and bioenergetic stress drive T_{PEX} cells propagating into early exhausted

[1]Institute for Immunology, Tsinghua University, Beijing, China. [2]Princess Margaret Cancer Centre, University Health Network, Toronto, Ontario, Canada. [3]China National Center for Bioinformation, Beijing, China. [4]State Key Laboratory of RNA Innovation, Science and Engineering, Beijing Institute of Genomics, Chinese Academy of Sciences, Beijing, China. [5]College of Future Technology, Sino-Danish College, University of Chinese Academy of Sciences, Beijing, China. [6]Karolinska Institutet, Stockholm, Sweden. [7]School of Basic Medical Sciences, Tsinghua Medicine, Tsinghua University, Beijing, China. [8]Beijing Key Laboratory of Immunological Research of Allergy (LIRA), Tsinghua University, Beijing, China. [9]State Key Laboratory of Molecular Oncology, School of Basic Medical Sciences, Tsinghua University, Beijing, China. [10]Departments of Immunology and Medical Biophysics, University of Toronto, Toronto, Ontario, Canada. [11]Centre for Oncology and Immunology, Hong Kong Science Park, Hong Kong SAR, China. [12]Department of Pathology, School of Clinical Medicine, Li Ka Shing Faculty of Medicine, The University of Hong Kong, Queen Mary Hospital, Hong Kong SAR, China. [13]These authors contributed equally: Yi Liu, Haochen Ni, Jie Li. ✉e-mail: handl@big.ac.cn; michellexu@mail.tsinghua.edu.cn

T cells (T_{EX}), which eventually differentiate into non-reprogrammable terminal T_{EX} cells[3,6,8]. Counteracting exhaustion traits to steer T cells toward the effector branch could thus rejuvenate T cell fitness and their therapeutic efficacy.

Chronic antigenic stimulation activates exhaustion-associated transcription and epigenetic programs controlled by transcription factors of the TOX and NR4A families, leading to a permanent loss of effector function[4,9]. Although most studies on T cell exhaustion have emphasized transcriptional regulation, the role of translational regulation remains underexplored. Emerging evidence suggests that during cellular stress, cells selectively allocate translational resources to specific pre-existing mRNAs, enabling rapid protein synthesis without continuous mRNA expression[10]. However, the specific changes in the translational landscape during the transition to T cell dysfunction and exhaustion, and the precise mRNAs prioritized for translation in T_{EX} cell differentiation, are still not fully understood.

In this study, we show that dysregulated translation in tumor-specific T cells drives both dysfunction and reduced persistence within tumors. We identify the RNA-binding protein (RBP) LARP4 as a regulator of hypertranslation in intratumoral T cells. LARP4 specifically enhances the translation efficiency (TE) of nuclear-encoded oxidative phosphorylation (OXPHOS) mRNAs, while leaving the synthesis of mitochondrial-encoded mRNAs unaffected, leading to an imbalanced OXPHOS subunit synthesis and mitochondrial dysfunction. Knockout (KO) of *Larp4* in tumor-specific $CD8^+$ T cells attenuates this hypertranslation, restores mitochondrial function, antagonizes exhaustion and re-engages T cell differentiation toward an effector state within the TME. These findings underscore the importance of translational regulation in maintaining T cell functionality within tumors and suggest that targeting LARP4 might be an effective strategy to enhance adoptive T cell therapies for solid tumors.

Results

Increased translational activity in T_{EX} cells in tumors

T cell exhaustion is characterized by distinct metabolic, transcriptional and epigenetic changes, but the role of translational regulation in this process remains largely unexplored. To investigate the impact of translation in T cell exhaustion, we used a well-established in vitro model in which naive mouse $CD8^+$ T cells (T_N) are exposed to chronic T cell receptor (TCR) stimulation via anti-CD3 antibody, driving their differentiation towards exhaustion[11] (Fig. 1a). After 4 days of in vitro culture, chronically stimulated T cells ('d4 T_{EX}') exhibited multiple exhaustive and dysfunctional features, including reduced effector functions, reduced mitochondrial activity and elevated expression of the inhibitory receptors PD-1 and TIM-3 compared to acutely stimulated functional $CD8^+$ T_{EFF} cells (Extended Data Fig. 1a–f). Extending TCR stimulation led to a continuous decline in effector functions (Extended Data Fig. 1a), a reduction in mitochondrial respiratory capacity and an increase in mitochondrial stress (Extended Data Fig. 1b,c). By day 8, most T cells co-expressed PD-1 and TIM-3 ('d8 T_{EX}') (Extended Data Fig. 1d–f), recapitulating the molecular phenotypes associated with T cell exhaustion. We assessed translation activity in these $CD8^+$ T cells using O-propargyl-puromycin (OPP), which integrates into nascent polypeptides and can be detected and quantified through flow cytometry[12]. In T_{EFF} cells, we observed a temporary increase in translation activity by day 4, followed by a decline by day 8 (Fig. 1b,c). By contrast, translation activity in T cells undergoing exhaustion showed a continuous rise. Chronically stimulated d8 T_{EX} cells exhibited significantly higher translation activity compared to both d4 T_{EX} cells and T_{EFF} cells (Fig. 1b,c).

We sought to determine whether the increased translation activity observed in T_{EX} cells in vitro could also be seen in tumor-infiltrating T_{EX} cells. To investigate this possibility, we subcutaneously inoculated C57BL/6J (B6) mice with ovalbumin (OVA)-expressing B16 melanoma cells (B16-OVA). After tumor establishment, we adoptively transferred naive OT-I T cells, which express TCRs specific for the OVA peptide 257–264 (ref. 13) (Fig. 1d). Consistent with previous findings[4,7,14,15], these tumor-specific T cells first differentiated into proliferation-competent T_{PEX} cells (PD-1^+ T_{PEX}) in the TdLNs. They gradually transitioned into early T_{EX} cells (PD-1^{hi} TIM-3^- early T_{EX}) and eventually into terminally exhausted cells (PD-1^{hi} TIM-3^+ terminal T_{EX}) within the TME (Fig. 1d and Extended Data Fig. 1g). Among the three T_{EX} subsets, T_{PEX} cells in the TdLNs exhibited the lowest level of translation activity, while terminal T_{EX} cells displayed the highest (Fig. 1e,f). These findings reveal that translation activity increases as tumor-specific T cells progress from T_{PEX} to terminal T_{EX} cells within the TME.

A low-input method for translatome profiling

Next, we aimed to profile active translation across tumor-specific T_{EX} subsets on a transcriptome-wide scale. However, existing methods requiring millions of cells render this impractical for studying T cells within tumors. To overcome this issue, we developed RPLace-seq, a ribosome profiling method optimized for low-input cells that integrates ribosome tagging (RiboTag)[16] with LACE-seq, a method for identifying the RNA bound to specific proteins[17]. RPLace-seq uses the RiboTag approach, in which hemagglutinin A (HA)-tagged ribosomal protein RPL22 is selectively expressed in the target cell type. This allows immunoprecipitation of ribosome-protected mRNA fragments for subsequent analysis by LACE-seq (Fig. 1g). Notably, the RPLace-seq cannot capture mitochondrial-encoded mRNAs owing to its reliance on HA-tagged RPL22 ribosomes (Extended Data Fig. 2a).

We performed this method alongside RNA-seq on 10^4 $CD8^+$ T_N cells and identified a comparable number of genes as RNA-seq (Fig. 1h). Ribosome-protected fragment (RPF) distribution from RPLace-seq exhibited characteristic features of ribosome profiling[18] (Fig. 1i,j and Extended Data Fig. 2b). Comparison with an independent polysome profiling dataset from $CD8^+$ T_N cells revealed strong correlation ($R^2 = 0.897$)[19] (Fig. 1k,l), confirming that RPLace-seq effectively captures actively translated polysome-bound mRNAs. By calculating the TE, we identified several known translational repressed mRNAs exhibiting lower TE than other mRNAs in $CD8^+$ T_N cells[19,20] (Fig. 1m and Extended Data Fig. 2c), validating the ability of RPLace-seq to accurately assess translational activities in T cells. These findings demonstrate the method's high precision and reliability for low-input cell analysis.

Profiling the translatome landscape of tumor-specific $CD8^+$ T cells

To further explore translatome dynamics in tumor-specific T cells, we applied RPLace-seq to 10^4 tumor-infiltrating OT-I T_{EX} (PD-1^{hi}) cells and OT-I T_{PEX} cells from TdLNs 21 days post transfer (Fig. 2a). RPLace-seq successfully captured an average of 10,822 and 13,120 genes in T_{PEX} and T_{EX} cells, respectively (Extended Data Fig. 3a), with high reproducibility in RPF abundance for both cell types ($R^2 = 0.992$ for T_{PEX} and $R^2 = 0.996$ for T_{EX}) (Extended Data Fig. 3b,c). When comparing RPF abundance between T_{EX} and T_{PEX} cells, we identified more upregulated transcripts ($n = 955$) than downregulated ones ($n = 686$), indicating that T_{EX} cells exhibit higher overall translation activity than T_{PEX} cells (Extended Data Fig. 3d). The similar increase in overall translation activity was recapitulated in T_{EX} cells induced in vitro (Extended Data Fig. 3e,f).

Given that the alternation of RPF abundance can be attributed to changes in mRNA levels, we analyzed the correlation between changes in RPF abundance and mRNA levels in T_{PEX} and T_{EX} cells. We found a weak correlation between mRNA and RPF levels ($R^2 = 0.257$), with nearly half of the RPF-upregulated transcripts (49.1%, 469 out of 955) showing no change in mRNA levels (Extended Data Fig. 3g,h). This discrepancy between mRNA and RPF levels may indicate changes in TE of specific genes rather than alterations in transcription. To explore this possibility, we compared TE across genes and identified 539 transcripts with significantly increased TE in T_{EX} cells compared to T_{PEX} cells. Notably, approximately 39.1% of these transcripts (211 out of 539), termed hypertranslated mRNAs, exhibited upregulation in both TE and RPF

https://doi.org/10.1038/s41590-025-02232-5

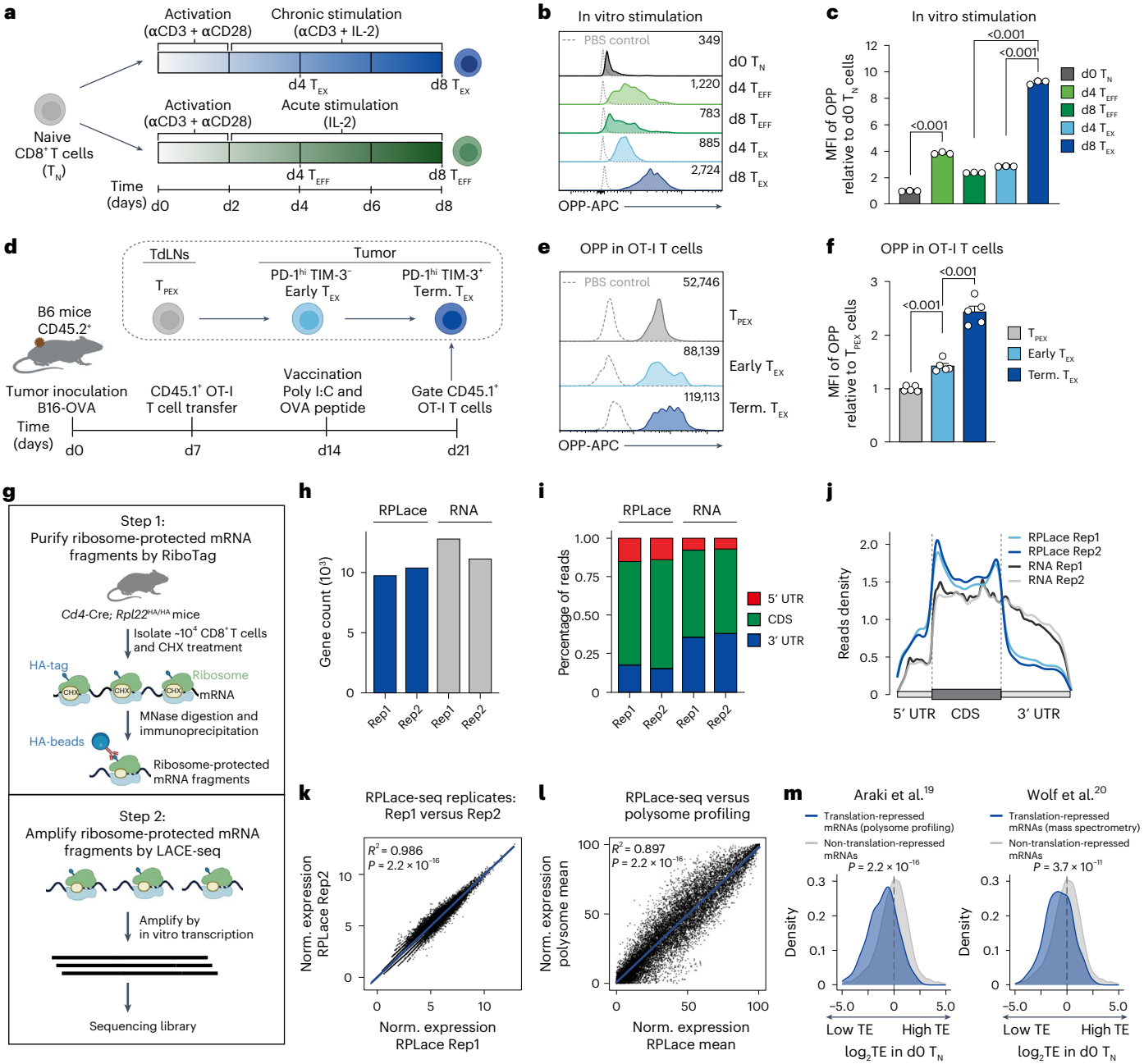

Fig. 1 | Increased global translation activity in exhausted CD8$^+$ T cells. **a**, Experimental timeline showing the differentiation of T_N cells into T_{EX} cells or T_{EFF} cells under in vitro chronic or acute antigenic (anti-CD3 antibody) stimulation for 8 days. **b**,**c**, Representative flow cytometry histograms (**b**) and bar plots (**c**) showing the OPP incorporation in T_N, T_{EFF} and T_{EX} cells ($n = 3$) under in vitro chronic or acute antigenic stimulation. The dashed lines in histograms represent the PBS control, and the mean fluorescence intensity (MFI) values are listed in the upper-right corner. **d**, Schematic diagram of in vivo experiment for gating T_{PEX}, early T_{EX} and terminal (term.) T_{EX}. A total of 1×10^6 B16-OVA cells were inoculated into B6 CD45.2$^+$ mice on day 0, followed by the transfer of 5×10^5 CD45.1$^+$ OT-I T cells on day 7. Mice were intratumorally injected with Poly I:C and OVA peptide 257–264 on day 14. T_{PEX} from TdLNs, early $T_{EX}$and terminal T_{EX} OT-I cells from the TME were analyzed on day 21. **e**,**f**, Representative flow cytometry histograms (**e**) and bar plots (**f**) showing the OPP incorporation in T_{PEX}, early T_{EX} and terminal T_{EX} OT-I cells ($n = 5$). The dashed lines in histograms represent the PBS control, and the MFI values are listed in the upper-right corner. **g**, Schematic diagram of the RPLace-seq workflow. CHX, cycloheximide. **h**, Gene count of mRNAs (transcripts per million > 0.5) identified by RPLace-seq and RNA-seq in CD8$^+$ T_N cells. A total of 1×10^5 CD8$^+$ T_N cells isolated from spleen and lymph nodes of *Cd4*-Cre; *Rpl22*$^{HA/HA}$ mice were used for RPLace-seq and RNA-seq. Rep1 and Rep2 are two biological replicates, namely, replicate 1 and replicate 2. **i**, Percentage of reads mapping to 5′ untranslated region (UTR), coding DNA sequence (CDS) region and 3′ UTR of transcripts in RPLace-seq and RNA-seq data. **j**, Metagene plot depicting the read distribution across 5′ UTR, CDS region and 3′ UTR of transcripts in RPLace-seq and RNA-seq data. **k**, Scatter plot comparing normalized (norm.) expression (rlog) of mRNAs between RPLace-seq replicates. Pearson correlation was used to assess agreement, and the coefficient of determination (R^2), P value (two-sided) and line of best fit are indicated. **l**, Scatter plot comparing the mean normalized expression (Rank-In) of mRNAs between RPLace-seq and polysome profiling data in CD8$^+$ T_N cells. Pearson correlation was used to assess agreement, and R^2, P value (two-sided) and line of best fit are indicated. **m**, Density plots showing the distribution of TE of translation-repressed mRNAs identified by polysome profiling (left) or mass spectrometry (right) and non-translation-repressed mRNAs in CD8$^+$ T_N cells. In **c**, n is the number of technical replicates; in **f**, n is the number of mice. For statistical analysis, bar plots in **c** and **f** are presented as means and were analyzed using unpaired two-sided Student's t-tests; error bars, s.e.m. Two-sided Kolmogorov–Smirnov test was performed for **m**. The data represent three independent experiments in **c** and **f**. Figures in **a**, **d** and **g** created with BioRender.com.

https://doi.org/10.1038/s41590-025-02232-5

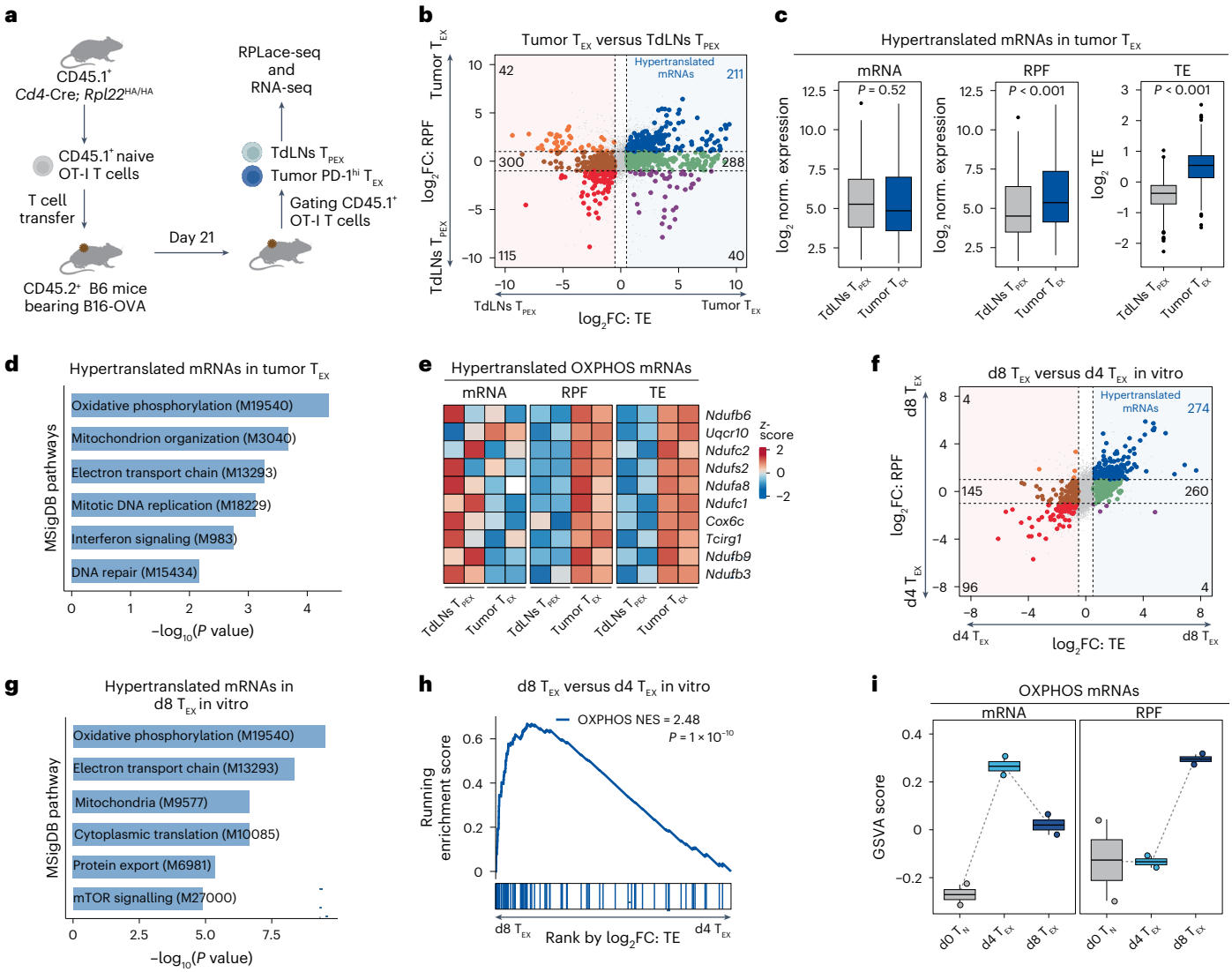

Fig. 2 | The translatome landscape of tumor-specific T cells. a, Schematic diagram for the experiment design to analyze the translatome in tumor-specific T cells using RPLace-seq and RNA-seq. CD45.1$^+$ OT-I T cells isolated from *Cd4*-Cre; *Rpl22*$^{HA/HA}$ mice were transferred into B6 mice bearing B16-OVA tumors. T_{PEX} cells and T_{EX} cells from TdLNs and tumors were collected on day 21 for RPLace-seq and RNA-seq analyses. Figure created with BioRender.com. **b**, Scatter plot comparing the $\log_2$ fold change ($\log_2$FC) in TE and RPF abundance between tumor T_{EX} cells and TdLNs T_{PEX} cells. The genes highlighted with a colored background indicate significant changes in TE ($|\log_2FC| > 0.5$, $P < 0.05$). The mRNAs with significantly changed TE were further divided into three groups based on the $\log_2$FC of RPF abundance: (i) less than −1, (ii) between −1 and 1 or (iii) greater than 1. Hypertranslated mRNAs (TE, $\log_2FC > 0.5$, $P < 0.05$; RPF, $\log_2FC > 1$) in tumor T_{EX} cells are indicated in blue. **c**, Box plots showing the mean normalized expression levels (rlog) of mRNA and RPF, as well as TE of hypertranslated mRNAs ($n = 211$) in tumor T_{EX} cells compared to TdLNs T_{PEX} cells. **d**, MSigDB pathway analysis of hypertranslated mRNAs in tumor T_{EX} cells. The systematic name of each pathway in MSigDB is labeled. **e**, Heatmap showing the relative levels of mRNA, RPF and TE of indicated hypertranslated OXPHOS mRNAs in TdLNs T_{PEX} cells and tumor T_{EX} cells. **f**, Scatter plot comparing the $\log_2$FC of TE and RPF abundance between d8 T_{EX} cells and d4 T_{PEX} cells under in vitro chronic antigenic stimulation. The genes highlighted with a colored background indicate significant changes in TE ($|\log_2FC| > 0.5$, $P < 0.05$). Hypertranslated mRNAs (TE, $\log_2FC > 0.5$, $P < 0.05$; RPF, $\log_2FC > 1$) in d8 T_{EX} cells are indicated in blue. **g**, MSigDB pathway analysis of hypertranslated mRNAs in d8 T_{EX} cells. The systematic name of each pathway in MSigDB is labeled. **h**, Gene set enrichment analysis to assess the enrichment of OXPHOS mRNAs in d8 T_{EX} cells or d4 T_{EX} cells. Transcripts were ranked based on $\log_2$FC of TE between d8 T_{EX} cells and d4 T_{PEX} cells. NES, normalized enrichment score. **i**, Box plots showing gene set variation analysis (GSVA) score of OXPHOS mRNAs based on the mRNA levels and RPF abundance in d0 T_N cells, d4 T_{EX} cells and d8 T_{EX} cells ($n = 2$). For statistical analysis, unpaired two-sided Student's *t*-tests were performed for **c** and **i**. The two-sided permutation test was performed for **h**. Box plots in **c** and **i** include the following elements: center line, median; box limits, upper and lower quartiles; whiskers, 1.5 × interquartile range (IQR) of the upper quartile and lower quartile.

abundance in T_{EX} cells, despite no corresponding changes in mRNA levels (Fig. 2b,c and Supplementary Table 1).

Pathway enrichment analysis using MSigDB gene sets revealed that these hypertranslated mRNAs were functionally enriched in pathways related to OXPHOS[21] (Fig. 2d,e). Specifically, 73.4% (58 out of 79) of OXPHOS mRNAs demonstrated increased TE in T_{EX} cells compared to T_{PEX} cells (Extended Data Fig. 3i). By contrast, the TE of exhaustion-associated molecules remained stable, despite elevated RPF abundance in T_{EX} cells compared to T_{PEX} cells (Extended Data Fig. 3j,k). Moreover, the hypertranslated mRNAs identified in d8 T_{EX} cells cultured in vitro also showed specific functional enrichment in the OXPHOS pathway (Fig. 2f–h and Supplementary Table 2). Specifically, OXPHOS mRNAs were expressed consistently in both d4 T_{EX} cells and d8 T_{EX} cells; however, extended antigen exposure resulted in an increase in the translation of these mRNAs in d8 T_{EX} cells by activating the translation of pre-existing transcripts (Fig. 2i). This pattern aligns with the concept

of 'translation on-demand', which enables rapid availability of proteins in response to specific signals without requiring continuous expression. Therefore, our findings from RPLace-seq reveal a translatome remodeling and TE-dependent hypertranslation in tumor-infiltrating T_{EX} cells. Moreover, the observed 'translation on-demand' of OXPHOS mRNAs in T_{EX} cells may be essential for their development.

LARP4 interacts with hypertranslated mRNAs in CD8$^+$ T_{EX} cells

Recent research indicates that RBPs function as selective regulators of translation by targeting specific pre-existing transcripts to influence their TE[22]. To identify candidate RBPs that might enhance the TE of hypertranslated mRNAs in T_{EX} cells, we extracted target transcripts of 150 RBPs from the ENCODE eCLIP-seq database[23]. Subsequently, we evaluated their enrichment with these hypertranslated mRNAs using Fisher's exact test (Extended Data Fig. 4a). Remarkably, the mRNA targets of LARP4 exhibited the most substantial enrichment with hypertranslated mRNAs in chronically stimulated d8 T_{EX} cells (Fig. 3a). Additionally, we observed that LARP4 protein levels were temporarily elevated in acutely stimulated T_{EFF} cells (Extended Data Fig. 4b,c), while LARP4 remained at consistently higher levels in chronically stimulated T_{EX} cells (Extended Data Fig. 4d), indicating that the expression of LARP4 in T cells is driven by chronic TCR stimulation.

We next investigated the regulation of *Larp4* expression in intratumoral T cells. *Larp4* was upregulated in intratumoral T_{EX} cells compared with the T_{PEX} cells in TdLNs (Extended Data Fig. 4e), and intratumoral terminal T_{EX} cells exhibited the highest expression compared with the less-exhausted subpopulation in mouse B16 melanoma cancer models[24] (Extended Data Fig. 4f). *LARP4* expression was also upregulated in T_{PEX} cells and T_{EX} cells from patients with melanoma compared with terminally differentiated effector memory T cells[25] (Extended Data Fig. 4g). Examination of ATAC-seq and CHIP-seq data revealed binding of the transcription factors TOX and NR4A1 to the *Larp4* loci (Fig. 3b and Extended Data Fig. 4h). We noticed that NR4A1 binds to an active enhancer region in T_{EX} cells, characterized by bi-directional transcription of enhancer RNA detected by PRO-seq (Fig. 3b). Furthermore, KO of *Nr4a1/2* rather than *Tox* significantly reduced *Larp4* expression levels in intratumoral T_{EX} cells (Extended Data Fig. 4i,j), indicating that *Larp4* expression is directly regulated by NR4A1/2.

To investigate whether the upregulated LARP4 directly interacts with hypertranslated mRNAs in T_{EX} cells, we conducted LACE-seq to analyze LARP4-targeted mRNAs under chronic antigenic stimulation in vitro. We found that LARP4 binding sites displayed the highest density near the stop codon (Fig. 3c and Supplementary Table 3), aligning with previous observations[26]. The mRNAs targeted by LARP4 demonstrated a significantly greater TE than non-targeted mRNAs in d8 T_{EX} cells, although this difference was not present in d4 T_{EX} cells (Fig. 3d). Further analysis of the fold change in TE between d4 T_{EX} cells and d8 T_{EX} cells indicated that the TE of LARP4-targeted mRNAs markedly increased in d8 T_{EX} cells compared to non-targeted mRNAs, as shown by the cumulative distribution analysis (Fig. 3e). Additionally, pathway enrichment analysis revealed that LARP4-targeted mRNAs were significantly enriched for genes involved in the OXPHOS pathway, including *Cox4i1* (Fig. 3f,g). We also observed that these LARP4-targeted OXPHOS mRNAs are nuclear-encoded, with no mitochondrial-encoded OXPHOS mRNAs identified as LARP4 targets (Extended Data Fig. 4k–n). Consistently, the TE of LARP4-targeted OXPHOS mRNAs significantly increased in d8 T_{EX} cells when compared to both LARP4-targeted non-OXPHOS mRNAs and non-LARP4-targeted mRNAs (Fig. 3h). These findings suggest that LARP4 interacts directly with hypertranslated mRNAs in T_{EX} cells, including nuclear-encoded OXPHOS mRNAs, but does not engage with mitochondrial-encoded mRNAs.

Growing evidence indicates that nuclear-encoded OXPHOS mRNAs can undergo local translation at the outer membrane of mitochondria, which allows for on-demand translation to support efficient mitochondrial biogenesis[27,28]. Considering that LARP4 does not use sequence-specific motifs for RNA recognition[26] (Extended Data Fig. 4o,p), we reasoned that LARP4 might localize near mitochondria in T_{EX} cells, enabling it to recognize these nuclear-encoded OXPHOS mRNAs. Through structured illumination microscopy, we observed LARP4 positioned closer to mitochondria within the cytoplasm in T_{EX} cells compared to T_{EFF} cells under in vitro antigenic stimulation (Fig. 3i). Furthermore, our analysis revealed that LARP4's targets were significantly enriched mitochondria-proximal mRNAs[28] (Extended Data Fig. 4q). Notably, the TE of these LARP4-targeted mitochondria-proximal mRNAs increased significantly in d8 T_{EX} cells (Fig. 3j). Overall, these findings suggest that LARP4 localizes near mitochondria and selectively targets hypertranslated mRNAs, particularly nuclear-encoded OXPHOS mRNAs, in exhausted CD8$^+$ T cells.

LARP4 drives hypertranslation in CD8$^+$ T_{EX} cells

To investigate whether LARP4 contributes to the increased TE observed in T_{EX} cells, we used CRISPR–Cas9 to knock out *Larp4* in T cells. We designed *Larp4*-targeting single guide RNA (sgRNA) (sg*Larp4*) and transduced it into activated CD8$^+$ T cells to create *Larp4*-KO cells. We included a control group that received a non-targeting sgRNA for comparison (control cells) (Extended Data Fig. 5a). After 8 days of in vitro chronic antigenic stimulation, *Larp4*-KO CD8$^+$ T_{EX} cells displayed significantly reduced translation activity, as indicated by decreased incorporation of OPP, compared to control CD8$^+$ T_{EX} cells (Fig. 3k,l). By contrast, overexpressing *Larp4* in CD8$^+$ T_{EX} cells resulted in a substantial increase in translation activity compared to control cells (Fig. 3k,l). Furthermore, knocking out *Nr4a1* and *Nr4a2*, upstream of *Larp4*, led to a marked decrease in global translation activity in CD8$^+$ T cells upon chronic antigenic stimulation (Extended Data Fig. 5b–d), suggesting that NR4A1/2-driven LARP4 expression is necessary to trigger hypertranslation in exhausted CD8$^+$ T cells.

To further explore whether LARP4 influences the translation activity of tumor-infiltrating T cells, we generated Cas9$^+$ OT-I mice by crossing Cas9 transgenic mice with OT-I mice (C9OT-I T cells). After transducing *Larp4*-sgRNAs (*Larp4*-KO C9OT-I) or control-sgRNAs (control C9OT-I) into C9OT-I T cells, we transferred these OT-I T cells into mice bearing B16-OVA tumors. Although *Larp4*-KO OT-I T cells exhibited similar translation activity to control cells in TdLNs, tumor-infiltrating *Larp4*-KO OT-I T cells displayed significantly reduced translation activity compared to their tumor-infiltrating control counterparts (Fig. 3m,n). These findings suggest that LARP4 drives an increase in translation activity of tumor-specific CD8$^+$ T cells within the TME.

To examine differences in the translatome, we conducted RPLace-seq alongside RNA-seq on *Larp4*-KO and control T_{EX} cells undergoing 8 days of chronic antigenic stimulation. *Larp4* KO significantly reduced the TE of LARP4-targeted mRNAs (Fig. 3o,p and Supplementary Table 4), without notably impacting their mRNA levels (Fig. 3q). Furthermore, a greater number of LARP4-targeted mRNAs displayed downregulated TE ($n = 204$), including *Cox4i1*, compared to those with upregulated TE ($n = 61$) following *Larp4* KO (Extended Data Fig. 5e). Pathway enrichment analysis indicated that these LARP4-targeted mRNAs with downregulated TE were significantly enriched for OXPHOS-related genes (Extended Data Fig. 5f). Polysome fractionation followed by qPCR analysis validated reduced TE of LARP4-targeted OXPHOS mRNAs (*Uqcrc1*, *Cox4i1*, *Cox6b1* and *Atp5b*) in *Larp4*-KO cells, while non-target mRNA (*Cox1*) remained unaffected (Extended Data Fig. 5g,h). Given the earlier findings from RPLace-seq, which demonstrated that OXPHOS mRNAs are hypertranslated in T_{EX} cells (Fig. 2b–i), we conclude that LARP4 directly recognizes these hypertranslated mRNAs, and this interaction enhances their TE in CD8$^+$ T_{EX} cells.

LARP4 drives mitochondrial dysfunction in tumor-specific CD8$^+$ T cells

Next, we explored whether LARP4-mediated hypertranslation of nuclear-encoded OXPHOS mRNAs influences mitochondrial function in

https://doi.org/10.1038/s41590-025-02232-5

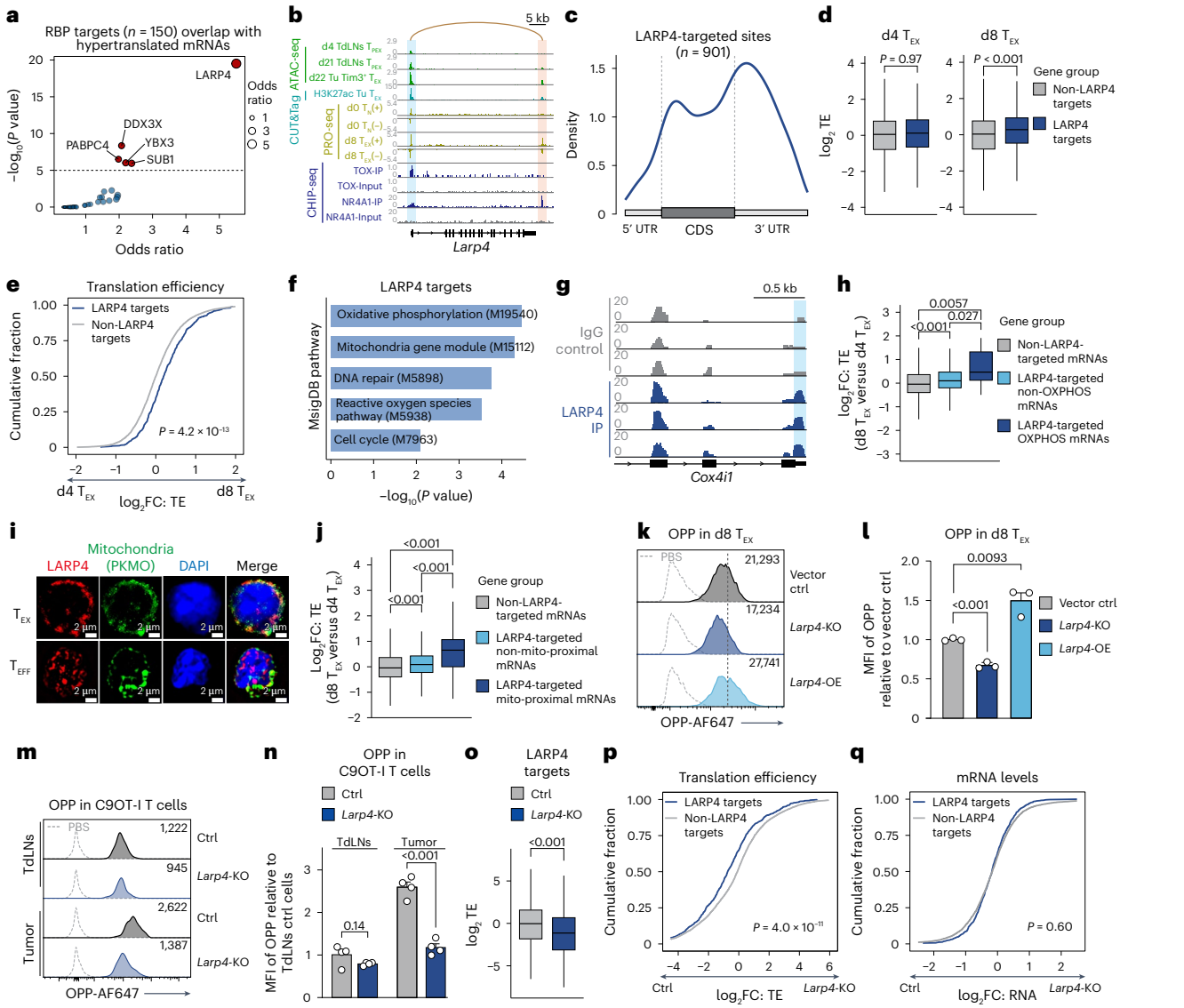

Fig. 3 | LARP4 interacts directly with hypertranslated mRNAs. a, Enrichment analysis for 150 RBP-targeted mRNA sets (eCLIP dataset from ENCODE database) overlapping with hypertranslated mRNAs in d8 T_{EX} cells. *P* value and odds ratio were calculated by Fisher's exact test. RBPs with $-\log_{10}$(*P* value) > 5 are labeled. **b**, Integrative Genomics Viewer tracks showing read distribution of ATAC-seq, CUT&Tag, PRO-seq and CHIP-seq at *Larp4* loci and the nearby enhancer region. The promoter and enhancer regions are highlighted with a colored background. Signal intensity of ATAC-seq for TdLNs T_{PEX} cells and tumor Ly108$^-$ TIM-3$^+$ T_{EX} cells, CUT&Tag for H3K27ac in tumor PD-1^{hi} TIM-3$^+$ T_{EX} cells, PRO-seq for d0 T_N cells and d8 T_{EX} cells and CHIP-seq for TOX and NR4A1 is shown. The activity-by-contact model was used to predict the potential regulation network in tumor T_{EX} cells based on the chromatin accessibility (ATAC-seq) and H3K27ac signal intensity (as well as genomic distance). **c**, Metagene plot depicting the distribution of LARP4-targeted sites across 5′ UTR, CDS region and 3′ UTR of transcripts. **d**, Box plot comparing the TE of LARP4-targeted mRNAs (LARP4 targets, *n* = 690) and non-LARP4-targeted mRNAs (non-LARP4 targets, *n* = 8692) in d4 T_{EX} cells and d8 T_{EX} cells. **e**, Cumulative fraction plot comparing $\log_2$FC of TE for LARP4 targets and non-LARP4 targets between d8 T_{EX} cells and d4 T_{EX} cells. **f**, MSigDB pathway analysis of LARP4 targets in d8 T_{EX} cells. The systematic name of each pathway in MSigDB is labeled. **g**, Representative Integrative Genomics Viewer tracks showing LARP4 binding to the OXPHOS mRNAs *Cox4i1* in d8 T_{EX} cells. Corresponding LARP4-binding regions are highlighted with a colored background. **h**, Box plot comparing the $\log_2$FC of TE for LARP4-targeted OXPHOS mRNAs (*n* = 15), LARP4-targeted non-OXPHOS mRNAs (*n* = 675) and non-LARP4-targeted mRNAs (*n* = 8,692) between d8 T_{EX} cells and d4 T_{EX} cells. **i**, Immunofluorescence of LARP4 co-localized with mitochondria in d8 T_{EX} cells and d3 T_{EFF} cells under in vitro antigenic stimulation. Mitochondria were stained with a probe for live cell mitochondria imaging (PKMO), and nuclei were stained with DAPI. **j**, Box plot comparing the $\log_2$FC of TE for LARP4-targeted mitochondria-proximal mRNAs (*n* = 58), LARP4-targeted non-mitochondria-proximal mRNAs (*n* = 632) and non-LARP4-targeted mRNAs (*n* = 8,692) between d8 T_{EX} cells and d4 T_{EX} cells. **k**,**l**, Representative flow cytometry histograms (**k**) and bar plots (**l**) showing OPP incorporation in T_{EX} cells transduced with sgRNA targeting *Larp4* (*Larp4*-KO), Larp4-vector (*Larp4*-OE) or control vector after 8 days of in vitro chronic antigenic stimulation. Dashed lines in histograms represent the PBS control, and MFI values are listed in the upper-right corner. OE, overexpression (*n* = 3). **m**,**n**, Representative flow cytometry histograms (**m**) and bar plots (**n**) showing OPP incorporation in *Larp4*-KO and control Cas9$^+$ OT-I (C9OT-I) T cells from TdLNs or tumors. Dashed lines in histograms represent the PBS control, and MFI values are listed in the upper-right corner (*n* = 4). **o**, Box plot comparing the mean TE of LARP4-targeted OXPHOS mRNAs (*n* = 690) between *Larp4*-KO and control T_{EX} cells after 8 days of in vitro chronic antigenic stimulation. **p**,**q**, Cumulative fraction plot comparing $\log_2$FC of TE (**p**) or mRNA levels (**q**) for LARP4-targeted mRNAs and non-LARP4-targeted mRNAs between *Larp4*-KO and control T_{EX} cells after 8 days of in vitro chronic antigenic stimulation. In **l**, *n* is the number of technical replicates; in **n**, *n* is the number of mice. For statistical analysis, two-sided Mann–Whitney *U*-tests were performed for **e**, **p** and **q**. Unpaired two-sided Student's *t*-tests were performed for **d**, **h**, **j**, **l**, **n** and **o**. Data in bar plots of **l** and **n** are shown as means; error bars, s.e.m. Box plots in **d**, **h**, **j** and **o** include the following elements: center line, median; box limits, upper and lower quartiles; whiskers, 1.5 × IQR of the upper quartile and lower quartile. The data represent two (**n**) or three (**i** and **l**) independent experiments.

T_{EX} cells. It has been demonstrated that the expression of mitochondrial protein and the number of mitochondria increase in tumor-specific T cells within the hypoxic TME, which links to higher production of mitochondrial reactive oxygen species (mtROS) and mitochondrial dysfunction[8,29]. We assumed that *Larp4* KO might reduce mitochondrial biogenesis and alleviate mtROS production. Indeed, a decrease in mitochondrial mass was observed in *Larp4*-KO T_{EX} cells compared to control T_{EX} cells (Extended Data Fig. 6a).

To compare the expression of mitochondrial protein upon *Larp4* KO, we measured the protein levels of two subunits of OXPHOS complex IV: COX4 (nuclear-encoded and targeted by LARP4) and COX1 (mitochondrial-encoded and not targeted by LARP4) (Extended Data Fig. 6b) in control and *Larp4*-KO $CD8^+$ T_{EX} cells that had undergone 8 days of chronic antigenic stimulation. We noticed that COX4 levels were significantly lower in *Larp4*-KO T_{EX} cells than in control T_{EX} cells, while overexpression of *Larp4* led to an increase in COX4 expression (Extended Data Fig. 6c). Conversely, COX1 expression remained relatively unaffected by either *Larp4* KO or overexpression (Extended Data Fig. 6c). Immunoblotting confirmed that the protein levels of these LARP4-targeted nuclear-encoded OXPHOS genes were reduced in chronically stimulated *Larp4*-KO $CD8^+$ T cells, while the level of mitochondrial-encoded OXPHOS proteins, such as ND4, CYTB and ATP6, remained largely unaffected (Fig. 4a).

Furthermore, we observed that *Larp4*-KO T_{EX} cells exhibited less mitochondrial stress than control T_{EX} cells. This was evidenced by lower levels of mtROS generation, measured using mitochondrial superoxide indicators (MitoSox) (Fig. 4b). By contrast, acutely stimulated *Larp4*-KO T_{EFF} cells exhibited mtROS levels comparable to control T_{EFF} cells (Fig. 4b). Notably, *Larp4* KO resulted in a significant improvement in respiratory activity among chronically stimulated T_{EX} cells (Fig. 4c) but had no effect on acutely stimulated T_{EFF} cells (Extended Data Fig. 6d). These results suggest that *Larp4* KO alleviates mitochondrial dysfunction in T_{EX} cells under in vitro chronic antigenic stimulation.

We speculated that the specific translational enhancement of nuclear-encoded OXPHOS subunits by LARP4 might contribute to mitochondrial dysfunction in T cells. To test this hypothesis, we overexpressed selected LARP4-targeted OXPHOS-related genes in activated $CD8^+$ T cells. The overexpression of LARP4-targeted OXPHOS mRNAs (*Cox4i1*, *Cox6b1* and *Atp5b*) led to increased mtROS levels in $CD8^+$ T cells at the early stage of chronic antigen stimulation (Fig. 4d). By contrast, overexpression of two non-LARP4-targeted OXPHOS mRNAs did not significantly increase mtROS levels (Fig. 4d), highlighting the role of LARP4-mediated translation of OXPHOS subunits in driving mitochondrial dysfunction in chronically stimulated T cells.

To investigate whether *Larp4* KO alleviates mitochondrial dysfunction in intratumoral T cells, we co-transferred equal numbers of congenically distinct *Larp4*-KO and control C9OT-I T cells into $Cas9^+$ B6 mice bearing B16-OVA tumors (Fig. 4e). Our findings revealed that *Larp4* KO specifically decreased the expression of the nuclear-encoded COX4 subunit in both C9OT-I PD-1^+ TIM-3^- T_{PEX} cells and PD-1^{hi} TIM-3^+ T_{EX} cells within the TME, while leaving mitochondrial-encoded COX1 unaffected (Fig. 4f). In addition, we observed that *Larp4*-KO PD-1^{hi} TIM-3^+ T_{EX} cells showed a decrease in mtROS generation compared to control T_{EX} cells in the TME (Fig. 4g), suggesting that mitochondrial fitness improves after *Larp4* KO. To evaluate mitochondrial activity relative to mitochondrial mass, we stained T cells with MitoTracker deep red and MitoTracker green, and subsequently calculated their ratio[8,30]. Notably, we found that the ratio of MitoTracker deep red to MitoTracker green in tumor-infiltrating PD-1^{hi} TIM-3^+ T_{EX} cells increased following *Larp4* KO (Fig. 4h), indicating that LARP4 negatively impacts mitochondrial activity in terminal T_{EX} cells within the TME. Collectively, these results suggest that LARP4 induces mitochondrial dysfunction in exhausted $CD8^+$ T cells within the TME.

LARP4-mediated translation of OXPHOS subunits drives T cell exhaustion

Mitochondrial dysfunction in tumor-infiltrating T cells can initiate exhaustion programs, ultimately resulting in a loss of T cell effector functions and promoting terminal differentiation toward exhaustion[8,31,32]. We reasoned that restoring mitochondrial function through *Larp4* KO could enhance the bioenergetic capacity and effector functions of tumor-specific $CD8^+$ T cells. To investigate the potential of modulating LARP4 to alleviate exhaustion, we chronically stimulated *Larp4*-KO and control $CD8^+$ T cells using anti-CD3 antibody under hypoxic conditions. Our results showed that *Larp4*-KO T cells expressed lower levels of inhibitory receptors and produced significantly higher amounts of cytokines than control T cells (Fig. 5a,b and Extended Data Fig. 7a).

Additionally, we found that overexpression of *Larp4* expedited the differentiation of T cells toward the terminally exhausted state (Extended Data Fig. 7b). Such an effect was abrogated when we overexpressed two *Larp4* mutants lacking either RNA binding activity (LARP4-M3) or ribosome interaction capacity (LARP4-ΔRIR)[33,34] (Extended Data Fig. 7c–g). By contrast, acutely stimulated control and *Larp4*-KO $CD8^+$ T cells displayed similar levels of activation and had comparable abilities to produce effector cytokines (Extended Data Fig. 7h–j), indicating that *Larp4* KO does not hinder T_{EFF} cell differentiation in vitro. Furthermore, the overexpression of LARP4-targeted OXPHOS subunits led to the upregulation of PD-1^{hi} TIM-3^+ $CD8^+$ T cell proportions, while the overexpression of *Uqcrfs1* and *Uqcrb1* only modestly increased the frequency of PD-1^{hi} TIM-3^+ cells (Fig. 5c and Extended Data Fig. 7k). These findings highlight the role of LARP4-mediated translation of OXPHOS subunits in driving T cell exhaustion in chronically stimulated T cells.

Larp4 KO restores effector function of tumor-specific T cells

To explore how *Larp4* KO alters the differentiation of tumor-specific $CD8^+$ T cells, we transferred control and *Larp4*-KO C9OT-I T cells into $Cas9^+$ B6 mice with B16-OVA tumors. We performed single-cell RNA sequencing (scRNA-seq) analysis on the tumor-infiltrating C9OT-I T cells 9 days post transfer (Fig. 5d). The KO of *Larp4* led to a significant increase in the proportion of tumor-infiltrating C9OT-I T cells (Fig. 5e). Six clusters of intratumoral C9OT-I T cells were identified based on signature genes[35–38] (Extended Data Fig. 7l,m and Supplementary Table 5). Although control cells primarily consisted of early and terminal T_{EX} cell subsets, *Larp4* KO reduced T_{EX} cell subsets and expanded T_{PEX} cells (Fig. 5f,g). Notably, *Larp4* KO resulted in a significant increase in effector memory T cells (T_{EM}) and *klrg1*-expressing effector-like T cell ($T_{EFF\text{-}like}$) subsets (Fig. 5f,g and Extended Data Fig. 7l,n). We found that $T_{EFF\text{-}like}$ cells and T_{EX} cells represent distinct differentiation pathways and identified a bi-directional differentiation path originating from the TCF1$^+$ T_{PEX} cell subset, which diverges into either the *Larp4*-KO cell-dominated effector path or Ctrl cell-dominated exhaustion path (Fig. 5h and Extended Data Fig. 7o,p). Moreover, *Larp4* KO significantly reduced the expression of exhaustion-driving transcription factor *Tox* and *Nr4a2* in T_{PEX} cells (Extended Data Fig. 7q), suggesting that *Larp4* modulates T cell differentiation as early as the T_{PEX} cell stage. These analyses highlight the dichotomy between T_{EX} cell and $T_{EFF\text{-}like}$ cell formation and emphasize the critical role that LARP4 has in counteracting the development of the effector branch.

Validation through flow cytometry revealed a significant increase in Ly108$^+$ TIM-3^- T_{PEX} cells, accompanied by a decrease in PD-1^{hi} TIM-3^+ terminal T_{EX} cells following *Larp4* KO (Fig. 5i,j). This reduction was further corroborated by a substantial decline in the proportion of cells expressing the exhaustion-driving transcription factor TOX in *Larp4*-KO C9OT-I T cells within the TME[39–41] (Fig. 5k). Additionally, we observed a notable increase in the proportion of CX3CR1$^+$ $T_{EFF\text{-}like}$ cells after *Larp4* KO[5,42] (Fig. 5l and Extended Data Fig. 8a–c). *Larp4*-KO C9OT-I T cells also produced higher levels of key cytokines, including

https://doi.org/10.1038/s41590-025-02232-5

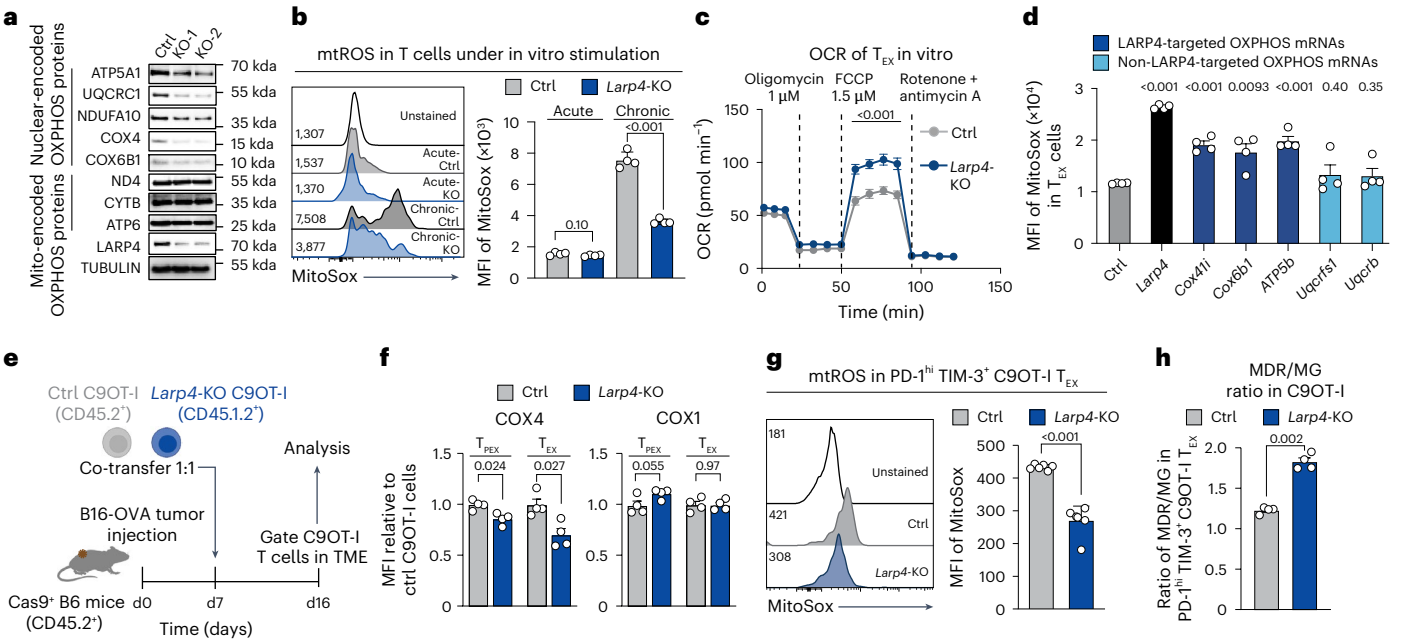

Fig. 4 | *LARP4* drives mitochondrial dysfunction in tumor-specific CD8⁺ T cells. **a**, Immunoblotting is shown to validate expression changes of proteins translated by LARP4-targeted nuclear-encoded OXPHOS mRNAs and non-LARP4-targeted mitochondrial-encoded OXPHOS mRNAs in control and *Larp4*-KO exhausted T cells after 8 days of in vitro chronic antigenic stimulation. **b**, Representative flow cytometry histograms (left) and bar plots (right) showing the levels of mtROS in control ($n = 4$) and *Larp4*-KO ($n = 4$) T cells under 8 days in vitro acute (T_{EFF}) or chronic (T_{EX}) antigenic stimulation, represented as the MFI of MitoSox staining. MFI values are indicated in the left corner of each histogram. **c**, Oxygen consumption rate (OCR) using the Seahorse XF bioanalyzer, measuring the respiratory capacity of control and *Larp4*-KO T_{EX} cells after 6 days of in vitro chronic antigenic stimulation. Cells were seeded at 5×10^5 cells per well in the XF96 plate ($n = 6$). FCCP, carbonyl cyanide *p*-(trifluoromethoxy) phenylhydrazone. **d**, Bar plots showing the levels of mtROS in cells overexpressing empty vector (Ctrl), *Larp4*, indicated LARP4-targeted OXPHOS mRNAs and indicated non-LARP4-targeted OXPHOS mRNAs after 6 days of in vitro chronic antigenic stimulation ($n = 4$). Statistical significance relative to control (ctrl) is indicated. **e**, Experimental design for co-transfer of control and *Larp4*-KO C9OT-I T cells into B16-OVA tumor-bearing mice. A total of 1×10^6 B16-OVA cells were subcutaneously inoculated into Cas9⁺ B6 mice. A total of 1×10^6 control and *Larp4*-KO C9OT-I T cells were intravenously co-transferred into Cas9⁺ B6 mice at a 1:1 ratio 7 days post tumor inoculation. The phenotypes of C9OT-I T cells were analyzed 9 days post T cell transfer. Figure created with BioRender.com. **f**, Bar plots showing MFI of COX4 and COX1 in both control and *Larp4*-KO C9OT-I PD-1⁺ TIM-3⁻ T_{PEX} cells and PD-1^{hi} TIM-3⁺ T_{EX} cells within the TME. The expression levels of COX proteins were measured using flow cytometry and normalized to the levels in control C9OT-I T cells ($n = 4$). **g**, Representative flow cytometry histograms and bar plots showing the levels of mtROS in chronically stimulated d8 T_{EX} cells from control ($n = 6$) and *Larp4*-KO ($n = 6$) groups, represented as the MFI of MitoSox staining. MFI values are indicated in the upper-left corner of each histogram. **h**, Bar plots showing the ratio of MitoTracker deep red (MDR) to MitoTracker green (MG) in control and *Larp4*-KO PD-1^{hi} TIM-3⁺ C9OT-I T_{EX} cells within the TME ($n = 4$). In **a**–**d**, *n* is the number of technical replicates; in **f**–**h**, *n* is the number of mice. For statistical analysis, data in **b**, **c**, **d**, **f**, **g** and **h** are presented as means; error bars, s.e.m. Unpaired two-sided Student's *t*-tests were performed for **b**–**d**; paired two-sided Student's *t*-tests were performed for **f**–**h**. The data represent two independent experiments in **a**–**d** and **f**–**h**.

TNF, IFNγ and IL-2 (Fig. 5m–o and Extended Data Fig. 8d–g), indicating a clear shift towards an effector phenotype in the absence of *Larp4*. Overall, our data suggest that LARP4 restricts the maintenance of T_{PEX} cells and drives CD8⁺ T cells toward a terminal exhaustion state, while simultaneously limiting their differentiation plasticity into an effector state within tumors.

Larp4 KO enhances T cell persistence and anti-tumor potency

To investigate whether LARP4 affects the persistence of tumor-specific CD8⁺ T cells within tumors[43], we transferred equal amounts of congenically distinct *Larp4*-KO and control C9OT-I T cells into Cas9⁺ B6 mice with B16-OVA tumors. We then assessed the ratio of *Larp4*-KO to control C9OT-I T cells in both TdLNs and the tumors. In the TdLNs, we found that the ratio of *Larp4*-KO to control C9OT-I T cells remained consistent at 1:1 (Fig. 6a). Furthermore, *Larp4* KO did not alter the development of T_{PEX} cells in TdLNs (Extended Data Fig. 9a,b). However, within the TME, this ratio gradually increased over time, indicating a preferential accumulation of *Larp4*-KO T cells compared to controls (Fig. 6b,c). Further analysis of C9OT-I T cell phenotypes revealed that *Larp4*-KO T cells within the tumors had a significantly lower proportion of T_{EX} cells and a higher proportion of T_{PEX} cells and $T_{EFF\text{-}like}$ cells compared to control C9OT-I T cells (Fig. 6d). These phenotypic differences were supported by a notable downregulation of the exhaustion-driving transcription factor TOX and an upregulation of the stemness-related transcription factor TCF1 in *Larp4*-KO T cells within the TME (Fig. 6e). These results suggest that knocking out *Larp4* enhances the persistence of tumor-specific CD8⁺ T cells within the TME.

Given the improved persistence and effector function of *Larp4*-KO T cells, we sought to evaluate their therapeutic potential. To determine whether *Larp4* KO could enhance the anti-tumor efficacy of tumor-specific CD8⁺ T cells and improve tumor control, we transferred *Larp4*-KO or control T cells into recipient Cas9⁺ B6 mice with B16-OVA tumors. We observed significantly better tumor control and prolonged survival in mice receiving *Larp4*-KO C9OT-I T cells compared to those receiving control C9OT-I T cells and PBS (Fig. 6f,g). These findings indicate that *Larp4* KO significantly enhances the persistence and anti-tumor potency of tumor-specific CD8⁺ T cells.

LARP4 knockdown enhances anti-tumor activity of CAR T cells

The exhaustion of CAR T cells caused by prolonged exposure to tumor antigens significantly limits their long-term efficacy in clinical settings[44–46]. We speculated that implementing an exhaustion-reversal strategy through LARP4 modulation in mouse models could also be

https://doi.org/10.1038/s41590-025-02232-5

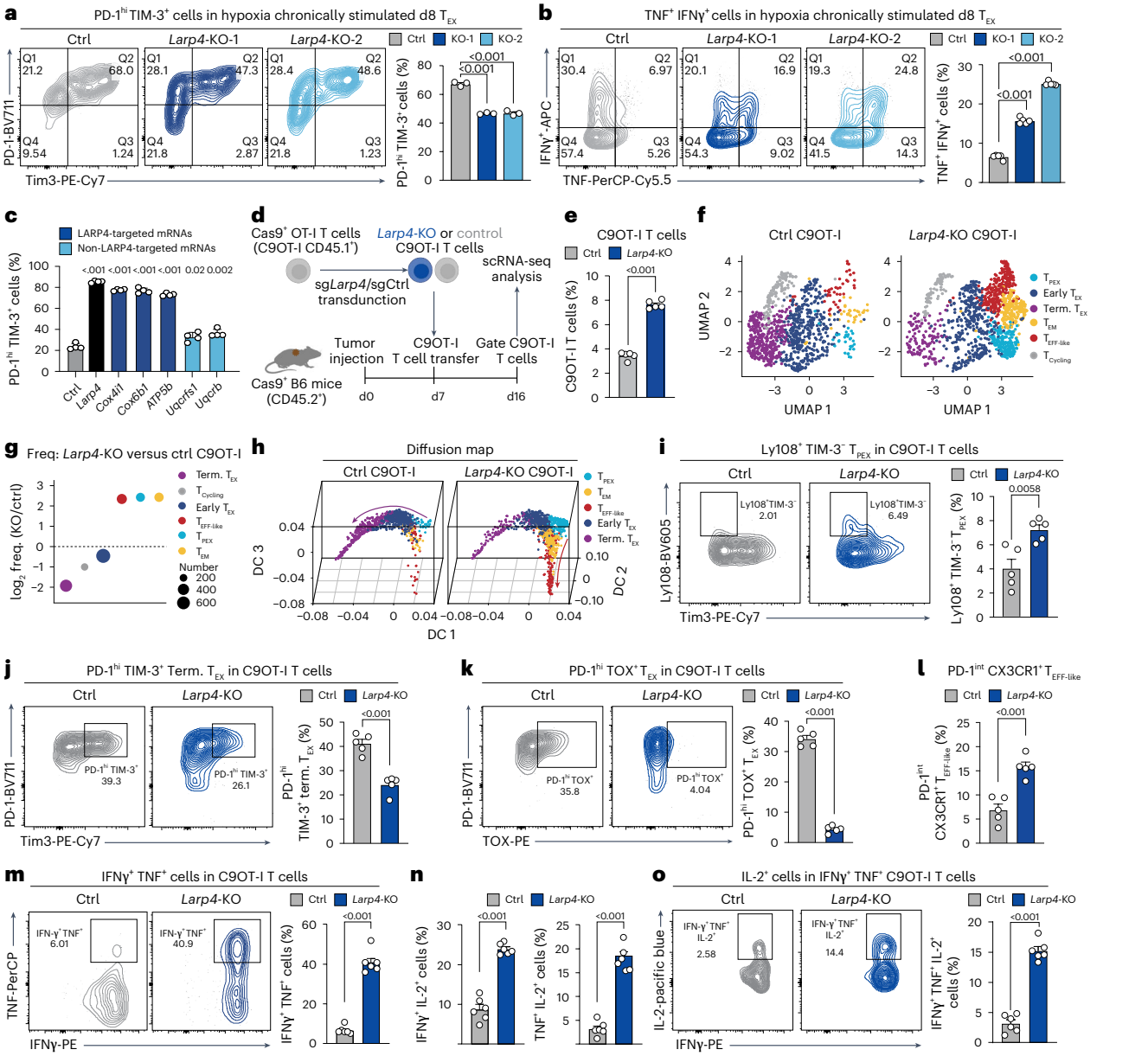

Fig. 5 | Knockout of *Larp4* alleviates T cell dysfunction within tumors. **a**,**b**, Representative flow cytometry graphs and bar plots showing the percentage of PD-1^{hi} TIM-3^{+} cells ($n = 3$) (**a**) and TNF^{+} IFNγ^{+} cells ($n = 5$) (**b**) in control and *Larp4*-KO T_{EX} cells after 8 days of in vitro chronic antigenic stimulation under hypoxic conditions. CD8^{+} T cells were isolated from Cas9^{+} B6 mice and activated with 2 μg ml^{-1} anti-CD3 and 1 μg ml^{-1} anti-CD28 antibody in normoxia (20% O_2). After 48 h, the T cells were resuspended and mixed with sgRNA-retroviral supernatant and then spin-transduced for 90 min. Subsequently, T cells were seeded at a concentration of 1×10^6 cells per ml on plates coated with 5 μg ml^{-1} anti-CD3 antibody and 10 ng ml^{-1} IL-2 under hypoxic conditions (2% O_2). The cells were passaged every 2 days. **c**, Bar plots showing the percentage of PD-1^{hi} TIM-3^{+} cells in cells overexpressing empty vector (Ctrl), *Larp4*, indicated LARP4-targeted OXPHOS mRNAs and indicated non-LARP4-targeted OXPHOS mRNAs after 6 days of in vitro chronic antigenic stimulation ($n = 4$). Statistical significance relative to ctrl is indicated. **d**, Schematic diagram for the analysis of C9OT-I T cells in Cas9^{+} B6 mice bearing B16-OVA tumors. A total of 1×10^6 B16-OVA cells were subcutaneously inoculated into Cas9^{+} B6 mice. A total of 1×10^6 control and *Larp4*-KO C9OT-I T cells were intravenously injected 7 days post tumor inoculation and collected from tumors for scRNA-seq 9 days post T cell transfer. Figure created with BioRender.com. **e**, Bar plots showing the percentage of control and *Larp4*-KO C9OT-I T cells in total CD8^{+} T cells within the TME ($n = 5$). **f**, Uniform manifold approximation and projection (UMAP) plot showing six subsets of control (left) and *Larp4*-KO (right) C9OT-I T cells within the TME. C9OT-I T cells were sorted 9 days post T cell transfer, followed by scRNA-seq. **g**, Dot plot depicting the relative frequency (freq.) of each subset between *Larp4*-KO and control C9OT-I T cells. **h**, Inferred differentiation trajectory among five subsets from scRNA-seq by diffusion map algorithm in control (left) and *Larp4*-KO (right) C9OT-I T cells. DC, diffusion component. **i**, Representative flow cytometry graphs and bar plots showing the percentage of Ly108^{+} TIM-3^{-} T_{PEX} cells in control and *Larp4*-KO C9OT-I T cells within the TME ($n = 5$). **j**, Representative flow cytometry graphs and bar plots showing the percentage of PD-1^{hi} TIM-3^{+} T_{EX} cells in control and *Larp4*-KO C9OT-I T cells within the TME ($n = 5$). **k**, Representative flow cytometry graphs and bar plots showing the percentage of PD-1^{hi} TOX^{+} T_{EX} cells in control and *Larp4*-KO C9OT-I T cells within the TME ($n = 5$). **l**, Bar plots showing the percentage of PD-1^{int} CX3CR1^{+} $T_{EFF\text{-}like}$ cells in control and *Larp4*-KO C9OT-I T cells within the TME ($n = 5$). PD-1^{int} CX3CR1^{+} $T_{EFF\text{-}like}$ cells were gated from PD-1^{+} TIM-3^{-} cells. **m**, Analysis of cytokine production in tumor-infiltrating C9OT-I T cells. Representative flow cytometry graphs and bar plots showing the percentage of IFNγ^{+} TNF^{+} cells in control and *Larp4*-KO C9OT-I T cells within the TME ($n = 6$). **n**, Bar plots showing the percentage of IFNγ^{+} IL-2^{+} and TNF^{+} IL-2^{+} cells in control and *Larp4*-KO C9OT-I T cells ($n = 6$). **o**, Representative flow cytometry graphs and bar plots showing the percentage of IFNγ^{+} TNF^{+} IL-2^{+} cells in control and *Larp4*-KO C9OT-I T cells ($n = 6$). In **a**–**c**, *n* is the number of technical replicates; in **e** and **i**–**o**, *n* is the number of mice. For statistical analysis, data in bar plots in **a**–**c**, **e** and **i**–**o** are presented as means and were analyzed using unpaired two-sided Student's *t*-tests; error bars, s.e.m. The data represent two (**a**, **b**, **c**, **m**, **n**, **o**) or three (**e**, **i**–**l**) independent experiments.

https://doi.org/10.1038/s41590-025-02232-5

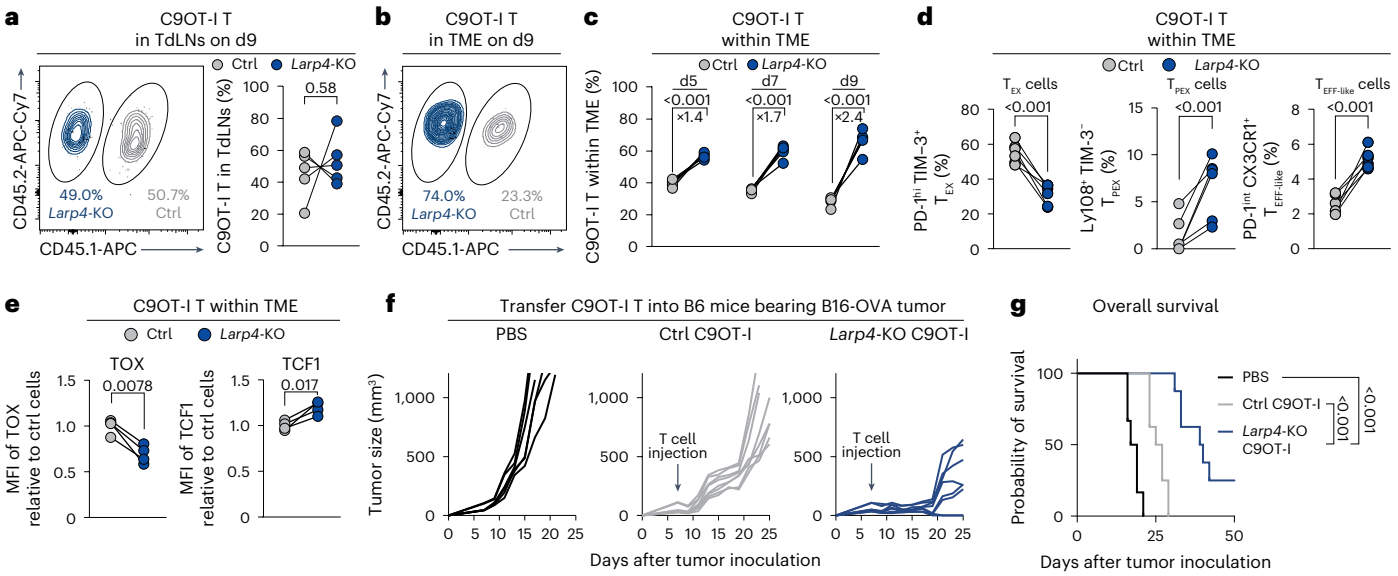

Fig. 6 | Knockout of *Larp4* in T cells enables sustained tumor control. **a**, Representative flow cytometry graphs and dot plots showing the percentage of control and *Larp4*-KO C9OT-I T cells in total transferred cells in TdLNs. A total of 1×10^6 control and *Larp4*-KO C9OT-I T cells were intravenously co-transferred into Cas9$^+$ B6 mice bearing a B16-OVA tumor at a 1:1 ratio 7 days after tumor inoculation. The phenotypes of C9OT-I T cells were analyzed 9 days following the transfer. The connecting lines in the dot plots illustrate comparisons between control and *Larp4*-KOT cells in the same tumor-bearing mice ($n = 5$). **b**, Representative flow cytometry graphs showing the percentage of control and *Larp4*-KO C9OT-I T cells in total transferred cells within the TME 9 days post T cell transfer. **c**, Dot plots showing the percentage of control and *Larp4*-KO C9OT-I T cells in total transferred cells within the TME 5, 7 and 9 days post T cell transfer, respectively. The connecting lines illustrate comparisons between control and *Larp4*-KO T cells in the same tumor-bearing mice ($n = 4$). **d**, Dot plots showing the percentage of PD-1^{hi} TIM-3$^+$ T_{EX} cells (left), Ly108$^+$ TIM-3$^-$ T_{PEX} cells (middle) and PD-1^{int} CX3CR1$^+$ $T_{EFF\text{-}like}$ cells (right) in total transferred control and *Larp4*-KO C9OT-I T cells within the TME 9 days post T cell transfer. The connecting lines illustrate comparisons between control and *Larp4*-KO cells in the same tumor-bearing mice ($n = 6$). **e**, Dot plots showing the levels of TOX (left) and TCF1 (right) in control and *Larp4*-KO C9OT-I T cells within the TME. The connecting lines illustrate comparisons between control and *Larp4*-KO T cells in the same tumor-bearing mice ($n = 4$). **f**, B16-OVA melanoma-engrafted Cas9$^+$ B6 mice were injected with the PBS ($n = 6$), 1×10^6 control C9OT-I T cells ($n = 8$) or 1×10^6 *Larp4*-KO C9OT-I T cells ($n = 8$) 7 days post tumor inoculation. Tumor volume was monitored over the indicated time period. Arrows indicate the date (day 7) of T cell injection. **g**, Kaplan–Meier overall survival curves for the Cas9$^+$ B6 tumor-bearing mice given the PBS ($n = 6$), control ($n = 8$) or *Larp4*-KO ($n = 8$) C9OT-I T cell injections. *n*, numbers of mice. For statistical analysis, paired two-sided Student's *t*-tests were performed for **a**, **c**, **d** and **e**. Two-sided Mantel–Cox test was performed for **g**. The data represent two (**a**, **c**, **e**) or three (**d**, **f**, **g**) independent experiments.

applied to human CAR T cells to sustain the anti-tumor activity of CAR T cells. We developed CD20-targeted CAR T cells aimed at treating B cell lymphoma. We knocked down *LARP4* using *LARP4*-shRNAs to create *LARP4*-KD CD20-CAR T cells, and we also established control CD20-CAR T cells using control-shRNA (Extended Data Fig. 9c). We observed that *LARP4*-KD CD20-CAR T cells exhibited significantly lower levels of inhibitory receptor expression (for example, TIM-3, CD39 and TIGIT) and mtROS production than control CD20-CAR T cells following prolonged tumor antigen stimulation[47] (Fig. 7a–d). Additionally, *LARP4* knockdown reduced the expression of nuclear-encoded OXPHOS genes, while the levels of mitochondrial-encoded OXPHOS genes remained unchanged (Fig. 7e).

In a CD20$^+$ Raji xenograft lymphoma model, mice that received a sub-therapeutic dose of *LARP4*-KD CD20-CAR T cells exhibited more significant tumor regression and longer survival than those that received control CD20-CAR T cells (Fig. 7f and Extended Data Fig. 9d). Importantly, this anti-tumor effect was also evident in a solid tumor model, as demonstrated in experiments involving mice with CD20-expressing colon cancer cells (MC38-hCD20) (Fig. 7g). Tumor-infiltrating *LARP4*-KD CD20-CAR T cells showed a substantial decrease in the expression of co-inhibitory receptors, including TIM-3 and TIGIT (Fig. 7h,i). Additionally, there was a reduced proportion of PD-1^{hi} TIM-3$^+$ T_{EX} cells in *LARP4*-KD CD20-CAR T cells compared to control CD20-CAR T cells (Fig. 7j,k). Collectively, these findings indicate that *LARP4* knockdown alleviates CAR T cell exhaustion, thereby enhancing their anti-tumor efficacy in vivo in both lymphoma and solid tumor contexts.

Discussion

Adoptive T cell therapies face significant challenges in treating solid tumors owing to compromised T cell fitness within bioenergetically deficient TMEs. Restoring intratumoral T cells to achieve durable, functional states remains a therapeutic hurdle. We demonstrate that abnormal translation regulation in intratumoral T cells drives T cell exhaustion and reduced persistence, highlighting a key mechanism that limits the effectiveness of T cell therapies. LARP4, as a critical translation regulator, selectively enhances the TE of nuclear-encoded OXPHOS mRNAs, contributing to mitochondrial dysfunction. Knocking out LARP4 in tumor-specific CD8$^+$ T cells (or knockdown in CAR T cells) mitigates hypertranslation, restores mitochondrial function and redirects T cells from dysfunctional toward a more effector-oriented branch. This rewiring enhances T cell durability and anti-tumor efficacy in solid tumors and lymphoma.

The transition of immune cells to new states in response to changing environmental signals often involves translation regulation and adaptive remodeling of the translatome[48]. These processes can complement and even override transcriptional control, allowing for a rapid response[48]. Our findings indicate that precise regulation of translation and the associated remodeling of the translatome are also essential for directing T cell fate toward dysfunction within tumors. This selective translation of specific genes—rather than a broad activation of translation—probably arises from competition among different mRNAs for access to translation machinery, including translation regulators and ribosomes[10]. Translation selectivity could also be mediated by coordinated interactions among multiple RBPs[22,49]. The spatial

https://doi.org/10.1038/s41590-025-02232-5

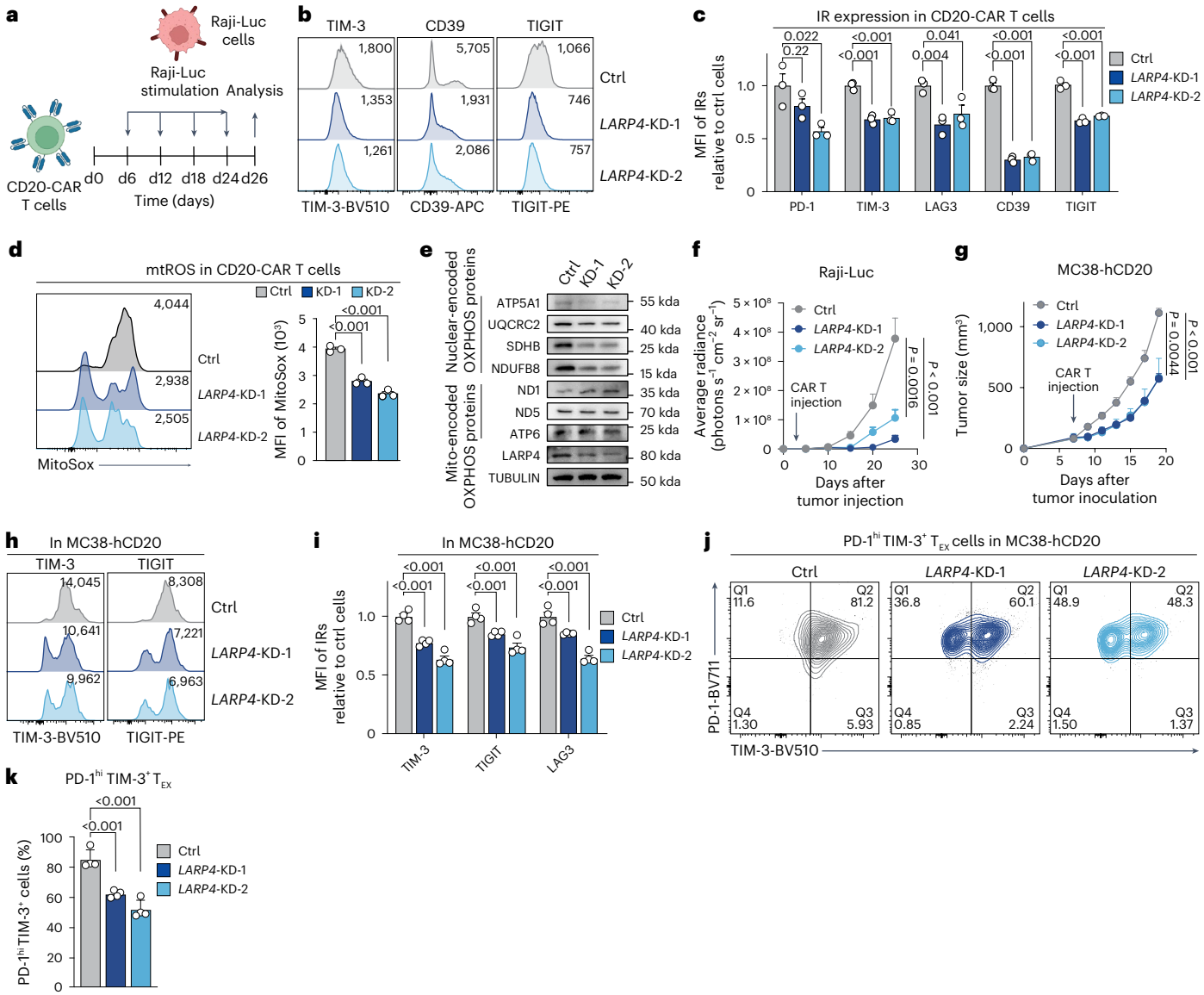

Fig. 7 | *LARP4* knockdown enhances anti-tumor activity of CAR T cells. **a**, Experimental design showing an in vitro repetitive stimulation assay for CD20-CAR T cells. A total of 3×10^5 CD20-CAR T cells were co-cultured with 1×10^5 irradiated Raji-Luc cells every 6 days. The CD20-CAR T cells were used for the following analysis on day 26. Figure created with BioRender.com. **b**, Representative flow cytometry histograms showing the expression of inhibitory receptors (IRs) TIM-3, CD39 and TIGIT in CD20-CAR T cells expressing shRNA against *LARP4* (*LARP4*-KD) or vector control (ctrl) after in vitro repetitive stimulation. **c**, Bar plots showing the expression of IRs (PD-1, TIM-3, LAG3, CD39, TIGIT) in control and *LARP4*-KD CD20-CAR T cells after in vitro repetitive stimulation. IR expression levels were measured by flow cytometry and normalized to control CD20-CAR T cells ($n = 3$). **d**, Representative flow cytometry histograms and bar plots showing the mtROS levels in control and *LARP4*-KD CD20-CAR T cells after in vitro repetitive stimulation. MFI values are indicated in the upper-right corner of each histogram ($n = 3$). **e**, Immunoblotting is shown to validate expression changes of nuclear-encoded OXPHOS proteins (including ATP5A1, UQCRC2, SDHB and NDUFB8) and mitochondrial-encoded OXPHOS proteins (including ND1, ND5 and ATP6) in control and *LARP4*-KD CD20-CAR T cells after in vitro repetitive stimulation. **f**, Average radiance of Raji-Luc cells in NCG mice injected with 5×10^5 control ($n = 9$), *LARP4*-KD-1 ($n = 9$) and *LARP4*-KD-2 ($n = 10$) CD20-CAR T cells. NCG mice were engrafted with 5×10^5 Raji-Luc cells by intraperitoneal injection. The arrow indicates the date (day 3) of T cell injection. The average radiance of Raji-Luc cells was measured every 5 days. **g**, Tumor growth of MC38-hCD20 colorectal tumor-engrafted mice injected with 5×10^5 control ($n = 10$), *LARP4*-KD-1 ($n = 10$) and *LARP4*-KD-2 ($n = 10$) CD20-CAR T cells. The arrow indicates the date (day 7) of T cell injection. The tumor size was measured every 2 days. **h**,**i**, Representative flow cytometry histograms (**h**) and bar plots (**i**) showing expression of IRs in tumor-infiltrating control and *LARP4*-KD CD20-CAR T cells ($n = 4$). **j**,**k**, Representative flow cytometry graphs (**j**) and bar plots (**k**) showing the percentage of PD-1^{hi} TIM-3$^+$ T_{EX} cells in tumor-infiltrating control and *LARP4*-KD CD20-CAR T cells ($n = 4$). In **c** and **d**, n is the number of technical replicates; in **f**, **g**, **i** and **k**, n is the number of mice. For statistical analysis, data are presented as means; error bars, s.e.m.; unpaired two-sided Student's *t*-tests were performed for **c**, **d**, **f**, **g**, **i** and **k**. The data represent two independent experiments in **c**–**g**, **i** and **k**.

co-compartmentalization of RBPs and certain groups of mRNAs leads to efficient localized translation, facilitating highly selective alternation in their TE[27,28,50]. Understanding the molecular mechanisms underlying the selective translation during the immune response, as well as identifying dysfunction-specific translation regulators instead of global regulators in T cells, could lead to innovative strategies for enhancing immunotherapies in cancers.

Our findings suggest that reducing translation activity through LARP4 modulation directly impacts T_{EFF} cell formation and counteracts the development of exhaustion. However, it remains uncertain whether

this translational regulation influences epigenetic imprinting in T_{EX} cells. It is plausible that LARP4-induced translatome remodeling is inherently linked to epigenetic reprogramming, resulting in a gradual loss of accessibility in open chromatin regions associated with the T_{PEX}–T_{EFF} lineage in tumor-infiltrating T_{EX} cells. Further research that integrates the molecular mechanisms of various regulatory layers governing the differentiation and persistence of T_{EX} cells will enhance our understanding and facilitate efforts to redirect T_{EX} populations toward a state of functional fitness within tumors.

Understanding how LARP4 regulates translation in $CD8^+$ T cells within the TME opens new avenues for enhancing T cell fitness by targeting translation factors. We propose that combining strategies to modulate LARP4 with functional enhancers for T cells could serve as a promising therapeutic approach. This combination may synergistically enhance the anti-tumor efficacy of adoptive T cell therapies, particularly in solid tumors.

Online content

Any methods, additional references, Nature Portfolio reporting summaries, source data, extended data, supplementary information, acknowledgements, peer review information; details of author contributions and competing interests; and statements of data and code availability are available at https://doi.org/10.1038/s41590-025-02232-5.

References

1. Albelda, S. M. CAR T cell therapy for patients with solid tumours: key lessons to learn and unlearn. *Nat. Rev. Clin. Oncol.* **21**, 47–66 (2024).
2. Baulu, E., Gardet, C., Chuvin, N. & Depil, S. TCR-engineered T cell therapy in solid tumors: state of the art and perspectives. *Sci. Adv.* **9**, eadf3700 (2023).
3. Zebley, C. C., Zehn, D., Gottschalk, S. & Chi, H. T cell dysfunction and therapeutic intervention in cancer. *Nat. Immunol.* **25**, 1344–1354 (2024).
4. Chow, A., Perica, K., Klebanoff, C. A. & Wolchok, J. D. Clinical implications of T cell exhaustion for cancer immunotherapy. *Nat. Rev. Clin. Oncol.* **19**, 775–790 (2022).
5. Beltra, J. C. et al. Stat5 opposes the transcription factor Tox and rewires exhausted $CD8^+$ T cells toward durable effector-like states during chronic antigen exposure. *Immunity* **56**, 2699–2718.e11 (2023).
6. Zehn, D., Thimme, R., Lugli, E., de Almeida, G. P. & Oxenius, A. 'Stem-like' precursors are the fount to sustain persistent $CD8^+$ T cell responses. *Nat. Immunol.* **23**, 836–847 (2022).
7. Connolly, K. A. et al. A reservoir of stem-like $CD8^+$ T cells in the tumor-draining lymph node preserves the ongoing antitumor immune response. *Sci. Immunol.* **6**, eabg7836 (2021).
8. Yu, Y. R. et al. Disturbed mitochondrial dynamics in $CD8^+$ TILs reinforce T cell exhaustion. *Nat. Immunol.* **21**, 1540–1551 (2020).
9. Baessler, A. & Vignali, D. A. A. T cell exhaustion. *Annu. Rev. Immunol.* **42**, 179–206 (2024).
10. Liu, Y., Beyer, A. & Aebersold, R. On the dependency of cellular protein levels on mRNA abundance. *Cell* **165**, 535–550 (2016).
11. Belk, J. A. et al. Genome-wide CRISPR screens of T cell exhaustion identify chromatin remodeling factors that limit T cell persistence. *Cancer Cell* **40**, 768–786.e7 (2022).
12. Signer, R. A., Magee, J. A., Salic, A. & Morrison, S. J. Haematopoietic stem cells require a highly regulated protein synthesis rate. *Nature* **509**, 49–54 (2014).
13. Wick, M. J. & Pfeifer, J. D. Major histocompatibility complex class I presentation of ovalbumin peptide 257–264 from exogenous sources: protein context influences the degree of TAP-independent presentation. *Eur. J. Immunol.* **26**, 2790–2799 (1996).
14. Schenkel, J. M. et al. Conventional type I dendritic cells maintain a reservoir of proliferative tumor-antigen specific $TCF\text{-}1^+$ $CD8^+$ T cells in tumor-draining lymph nodes. *Immunity* **54**, 2338–2353.e6 (2021).
15. Miller, B. C. et al. Subsets of exhausted $CD8^+$ T cells differentially mediate tumor control and respond to checkpoint blockade. *Nat. Immunol.* **20**, 326–336 (2019).
16. Sanz, E. et al. Cell-type-specific isolation of ribosome-associated mRNA from complex tissues. *Proc. Natl Acad. Sci. USA* **106**, 13939–13944 (2009).
17. Su, R. et al. Global profiling of RNA-binding protein target sites by LACE-seq. *Nat. Cell Biol.* **23**, 664–675 (2021).
18. Ingolia, N. T., Ghaemmaghami, S., Newman, J. R. & Weissman, J. S. Genome-wide analysis in vivo of translation with nucleotide resolution using ribosome profiling. *Science* **324**, 218–223 (2009).
19. Araki, K. et al. Translation is actively regulated during the differentiation of $CD8^+$ effector T cells. *Nat. Immunol.* **18**, 1046–1057 (2017).
20. Wolf, T. et al. Dynamics in protein translation sustaining T cell preparedness. *Nat. Immunol.* **21**, 927–937 (2020).
21. Castanza, A. S. et al. Extending support for mouse data in the Molecular Signatures Database (MSigDB). *Nat. Methods* **20**, 1619–1620 (2023).
22. Ho, J. J. D. et al. A network of RNA-binding proteins controls translation efficiency to activate anaerobic metabolism. *Nat. Commun.* **11**, 2677 (2020).
23. Van Nostrand, E. L. et al. A large-scale binding and functional map of human RNA-binding proteins. *Nature* **583**, 711–719 (2020).
24. Zhou, P. et al. Single-cell CRISPR screens in vivo map T cell fate regulomes in cancer. *Nature* **624**, 154–163 (2023).
25. Pauken, K. E. et al. Single-cell analyses identify circulating anti-tumor CD8 T cells and markers for their enrichment. *J. Exp. Med.* **218**, e20200920 (2021).
26. Lewis, B. M. et al. LARP4 is an RNA-binding protein that binds nuclear-encoded mitochondrial mRNAs to promote mitochondrial function. *RNA* **30**, 223–239 (2024).
27. Matsumoto, S. et al. Localization of mRNAs encoding human mitochondrial oxidative phosphorylation proteins. *Mitochondrion* **12**, 391–398 (2012).
28. Fazal, F. M. et al. Atlas of subcellular RNA localization revealed by APEX-seq. *Cell* **178**, 473–490.e26 (2019).
29. Vardhana, S. A. et al. Impaired mitochondrial oxidative phosphorylation limits the self-renewal of T cells exposed to persistent antigen. *Nat. Immunol.* **21**, 1022–1033 (2020).
30. Pendergrass, W., Wolf, N. & Poot, M. Efficacy of MitoTracker green and CMXrosamine to measure changes in mitochondrial membrane potentials in living cells and tissues. *Cytometry A* **61**, 162–169 (2004).
31. Lisci, M. & Griffiths, G. M. Arming a killer: mitochondrial regulation of $CD8^+$ T cell cytotoxicity. *Trends Cell Biol.* **33**, 138–147 (2023).
32. Scharping, N. E. et al. Mitochondrial stress induced by continuous stimulation under hypoxia rapidly drives T cell exhaustion. *Nat. Immunol.* **22**, 205–215 (2021).
33. Yang, R. et al. La-related protein 4 binds poly(A), interacts with the poly(A)-binding protein MLLE domain via a variant PAM2w motif, and can promote mRNA stability. *Mol. Cell. Biol.* **31**, 542–556 (2011).
34. Ranjan, A. et al. The short conserved region-2 of LARP4 interacts with ribosome-associated RACK1 and promotes translation. *Nucleic Acids Res.* **53**, gkaf053 (2025).
35. Siddiqui, I. et al. Intratumoral $Tcf1^+PD\text{-}1^+CD8^+$ T cells with stem-like properties promote tumor control in response to vaccination and checkpoint blockade immunotherapy. *Immunity* **50**, 195–211.e10 (2019).

36. Chu, Y. et al. Pan-cancer T cell atlas links a cellular stress response state to immunotherapy resistance. *Nat. Med.* **29**, 1550–1562 (2023).
37. Kowalczyk, M. S. et al. Single-cell RNA-seq reveals changes in cell cycle and differentiation programs upon aging of hematopoietic stem cells. *Genome Res.* **25**, 1860–1872 (2015).
38. Zilionis, R. et al. Single-cell transcriptomics of human and mouse lung cancers reveals conserved myeloid populations across individuals and species. *Immunity* **50**, 1317–1334.e10 (2019).
39. Alfei, F. et al. TOX reinforces the phenotype and longevity of exhausted T cells in chronic viral infection. *Nature* **571**, 265–269 (2019).
40. Scott, A. C. et al. TOX is a critical regulator of tumour-specific T cell differentiation. *Nature* **571**, 270–274 (2019).
41. Khan, O. et al. TOX transcriptionally and epigenetically programs $CD8^+$ T cell exhaustion. *Nature* **571**, 211–218 (2019).
42. Hashimoto, M. et al. PD-1 combination therapy with IL-2 modifies $CD8^+$ T cell exhaustion program. *Nature* **610**, 173–181 (2022).
43. Granhoj, J. S. et al. Tumor-infiltrating lymphocytes for adoptive cell therapy: recent advances, challenges, and future directions. *Expert Opin. Biol. Ther.* **22**, 627–641 (2022).
44. Long, A. H. et al. 4-1BB costimulation ameliorates T cell exhaustion induced by tonic signaling of chimeric antigen receptors. *Nat. Med.* **21**, 581–590 (2015).
45. Sterner, R. C. & Sterner, R. M. CAR-T cell therapy: current limitations and potential strategies. *Blood Cancer J.* **11**, 69 (2021).
46. Grosser, R., Cherkassky, L., Chintala, N. & Adusumilli, P. S. Combination Immunotherapy with CAR T cells and checkpoint blockade for the treatment of solid tumors. *Cancer Cell* **36**, 471–482 (2019).
47. Zhang, H. et al. A chimeric antigen receptor with antigen-independent OX40 signaling mediates potent antitumor activity. *Sci. Transl. Med.* **13**, eaba7308 (2021).
48. Marchingo, J. M. & Cantrell, D. A. Protein synthesis, degradation, and energy metabolism in T cell immunity. *Cell Mol. Immunol.* **19**, 303–315 (2022).
49. Hentze, M. W., Castello, A., Schwarzl, T. & Preiss, T. A brave new world of RNA-binding proteins. *Nat. Rev. Mol. Cell Biol.* **19**, 327–341 (2018).
50. Lesnik, C., Golani-Armon, A. & Arava, Y. Localized translation near the mitochondrial outer membrane: an update. *RNA Biol.* **12**, 801–809 (2015).

Methods

Mice

Specific-pathogen-free B6 mice were purchased from Charles River Laboratories. All mice were used in accordance with Tsinghua University Animal Ethics Committee guidelines. B6N.129-*Rpl22*$^{tm1.1Psam}$/J (RiboTag) mice were procured from the Jackson Laboratory (Jax; strain no. 011029). The RiboTag mouse was bred to a CD4-Cre recombinase-expressing mouse line to generate double homozygous mice for RPLace-seq-related experiments[16]. B6N.129(Cg)-*Gt(ROSA)26Sor*$^{tm1.1(CAG-cas9*,-EGFP)Fezh}$/J (Cas9$^+$) mice were bred in-house (Jax, 026430). OT-I mice (Jax, 003831) were crossed with Cas9$^+$ mice and then bred in-house. Male and female mice, aged 8–12 weeks, were used for experimentation. Tumor xenograft studies were conducted using NCG (NOD/ShiLtJGpt-*Prkdc*^{em26Cd52}*Il2rg*^{em26Cd22}/Gpt) mice aged 8–10 weeks (Gempharmatech). Mice were maintained under a 12 h light–dark cycle. All mice were housed under specific-pathogen-free conditions and were used in accordance with Tsinghua University Animal Ethics Committee guidelines.

Cell lines and culture conditions

B16-OVA is an OVA-transfected clone from the mouse melanoma cell line B16-F10 (ATCC, CRL-6475) as previously described[51]. MC38 was infected with a lentivirus expressing human CD20 and subcloned by limited dilution to generate MC38-hCD20. The 293T cell line was purchased from ATCC. Platinum-E cells were a kind gift from H. Qi's laboratory at Tsinghua University. All cell lines were verified to be mycoplasma-negative, and cell lines were maintained in DMEM with 10% FBS, L-glutamine, HEPES and NEAA. The Raji-luciferase (Raji-Luc) cell line expresses firefly luciferase and was cultured in RPMI 1640 (Gibco) containing 10% heat-inactivated FBS, 2 mM L-glutamine and 10 mM HEPES (Thermo Fisher).

Primary mouse T cell isolation and activation

Polyclonal or OT-I CD8$^+$ T cells were isolated from the spleen and lymph nodes using EasySep kits. Polyclonal cells were activated with plate-bound anti-CD3/CD28 and IL-2 (50 U ml^{-1}) for 48 h. OT-I cells were pulsed with 1 μM SIINFEKL for 1 h, then cultured in RPMI with supplements for 48 h. CD8$^+$ purity was confirmed by flow cytometry.

Acute and chronic antigenic T cell stimulation

Chronic T cell stimulation was performed as previously described with slight modifications[11,29]. After 48 h of initial activation, polyclonal and OT-I CD8$^+$ T cells were cultured at 1×10^6 cells per ml in RPMI with 10% FBS, glutamine, β-mercaptoethanol and IL-2 (10 ng ml^{-1}), with or without anti-CD3 (5 μg ml^{-1}) for chronic or acute stimulation, respectively. Cells were passaged every 48 h for 8 days. For sgRNA transduction, T cells were plated under hypoxia (2% O_2) with IL-2 and anti-CD3.

OPP assay

The OPP assay was performed as previously described with slight modifications[12]. For the protein synthesis quantification in vivo, OPP (50 μM) was used to pulse 1×10^6 tumor or draining lymph node single-cell suspensions for 1 h. The cells were fixed and stained with surface marker antibodies before being permeabilized. Detection of OPP was achieved using the Click-iT Cell Reaction Buffer Kit (Thermo) and analyzed by flow cytometry.

Retroviral production and T cell transduction

Retroviruses were generated in 293T cells using MSCV (Addgene, 24828) and pCL-Eco (Addgene, 12371) plasmids with PEI (MW40,000, YEASEN) as previously described[5]. Retroviral transduction was performed as previously described with slight modifications[52,53]. OT-I CD8$^+$ T cells were activated with SIINFEKL (1 μM) and rhIL-2 (100 U ml^{-1}), then spin-infected 24 h later with retrovirus and polybrene (4 μg ml^{-1}). GFP$^+$ cells were sorted the next day. CD45.2$^+$ or CD45.1.2$^+$ OT-I cells transduced with control or LARP4-RVs were mixed (5×10^5 each) and transferred into mice 7 days post B16-OVA implantation[54].

Tumor growth and treatment

B16-OVA cells (~80% confluent) were trypsinized, and 5×10^5 cells were injected subcutaneously into Cas9$^+$ or B6 mice. OT-I T cells were transferred on day 7. Tumor volume was determined as $(a \times b^2) / 2$. For the MC38-hCD20 model, 5×10^5 MC38-hCD20 tumor cells were inoculated into the flank of the mice[55]. Mice with MC38-hCD20 or B16-OVA tumors smaller than 1,000 mm^3 were considered to be surviving[29]. In the Raji-Luc xenograft model, NCG mice were injected intraperitoneally with 5×10^5 Raji-Luc cells. On day 3, mice were grouped based on in vivo bioluminescence imaging and treated with 5×10^5 CD20-CAR T cells by intravenous injection. Tumor burden was monitored every 5 days using a PerkinElmer IVIS Spectrum[55,56].

Plasmid construction

The sgRNA sequences used to generate the KO cell lines are listed in Supplementary Table 6. *Larp4* and control sgRNA were cloned into pMYS-U6-GFP (Addgene, 85451) and confirmed using Sanger sequencing[57]. The LARP4 construct has been described previously[58] and the pMSCV vector was kindly provided by M. Xu (National Institute of Biological Sciences). CAR lentiviral plasmids were constructed by cloning the rituximab-derived anti-hCD20 scFv, CD8 hinge/TM, 4-1BB and CD3ζ domains into a modified pCDH-EF1a vector. hCD20 cDNA was cloned into pCDH-EF1a-IRES-Puro.

Lentivirus production and transduction of human T cells

Lentivirus was produced as previously described[47]. Supernatants containing lentivirus particles were collected 48 h and 72 h after transfection. Transduction of human T cells was performed as described with slight modifications[47]. Total T cells were purified with the EasySep Human T Cell Isolation Kit (STEMCELL). T cell activation in culture was induced by plate-bound anti-CD3 and soluble anti-CD28 antibodies for 2 days, and then CAR-containing lentiviruses were transduced and cultured with RPMI 1640 complete medium supplemented with rhIL-2 (50 IU ml^{-1}). All experiments were approved by the Ethics Committee of Beijing Institute of Genomics, Chinese Academy of Sciences (2020S012).

Repetitive stimulation assay

The repetitive stimulation assay was performed as previously described[47]. In brief, irradiated (100 Gy) Raji-Luc cells were co-cultured with CAR T cells at a 1:3 R:T ratio every 6 days throughout the entire culture period. T cells were collected and counted every 2 days. On day 25 after the indicated stimulation, the CAR T cells were used for cytotoxicity, T cell subtype and exhaustion marker analysis.

Seahorse XF96 respirometry

Bioenergetics in T cells was measured using a Seahorse XF96 as previously described[59,60]. XF96 plates were coated with poly-D-lysine and seeded with 5×10^5 T cells per well overnight. OCR was measured using the XF96 Extracellular Flux Analyzer and Glucose Stress Fuel Flex Test kit (Agilent) per the manufacturer's protocol. Data were analyzed with Wave software.

Flow cytometry and cell sorting

Cells were blocked with Fc Block (2.4G2, BioX Cell) and stained with surface antibodies on ice. For intracellular staining, cells were fixed and permeabilized (BioLegend), then stained with intracellular antibodies or transcription factor buffers (Invitrogen). Data were acquired on a BD Fortessa and analyzed with FlowJo. For sorting, cells were stained and isolated using a BD FACS Aria III. RNA was extracted (RNeasy Plus Micro Kit, QIAGEN) for RNA-seq or RPLace-seq.

Polysome profiling and qPCR quantification

Ribosome profiling was performed as previously described with slight modifications[61]. Following fractionated of the gradients into ~200 µl fractions, absorbance (OD_{260}) profiles were acquired using a Nanodrop, and the polysome and non-polysome fractions were pooled based on absorbance curves. RNA was purified with a Zymo RNA Clean & Concentrator-5 kit. For qPCR with reverse transcription, cDNA was synthesized using EasyScript One-Step gDNA Removal and cDNA Synthesis SuperMix (TransGen). The quantities were determined with PerfectStart Green qPCR SuperMix (TransGen) on a CFX96 Touch system (Bio-Rad). Target gene expression was normalized to *Gapdh* using the $2^{-\Delta\Delta Ct}$ method.

RPLace-seq and LACE-seq

We established *Rpl22*-HA transgenic mice as previously described[16]. For RPLace-seq, cells isolated from tumor growth or adoptive transfer assays were treated with 100 µg ml^{-1} cycloheximide (Sigma-Aldrich) for 6 min at 37 °C. Cells were lysed and pre-cleared with protein A beads. A portion (1/20) of each lysate was used to extract total RNA by RNeasy Plus Micro Kit (QIAGEN) for subsequent RNA-seq, using SMARTer Stranded Total RNA-Seq Kit v2 (Clontech) according to the manufacturer's protocol. The remaining lysate was co-immunoprecipitated with anti-HA Magnetic Beads (Pierce) for 1 h at 4 °C. Samples were washed with lysis buffer and fragmented into segments of about 150 nucleotides with Micrococcal Nuclease (NEB). RPLace-seq was developed from LACE-seq[17] for low-input samples with some modifications. In brief, RNA was dephosphorylated and ligated with a 3′ linker. Then, RNA was reverse transcribed by Superscript IV (Thermo Fisher) with a biotinylated T7-RT primer. The first-strand cDNA was released from the beads and captured by Streptavidin C1 Dynabeads (Thermo Fisher). Cycloheximide must be added to buffers until the first strand of cDNA is captured. cDNA was ligated with a 3′ cDNA linker for pre-amplifying the double-stranded DNA fragments by PCR. Subsequently, the products were purified and used for T7 RNA polymerase (NEB)-based in vitro transcription. The RNA was reverse transcribed and sent to ZapR-mediated removal of rRNA (Clontech), followed by library construction for deep sequencing (from 130 to 300 bp). Paired-end sequencing (150 bp) of each RNA library was performed on a DNBSEQ-T7 platform (MGI). It should be noted that RPLace-seq relies on HA-tagged RPL22 for ribosome capture and therefore cannot detect mitochondrial ribosome-mediated translation events.

For LACE-seq, chronically stimulated T cells were irradiated twice with UV-C light on ice at a dose of 400 mJ. Protein A/G magnetic beads were resuspended in Larp4 antibody and incubated with gentle rotation at 4 °C for 1 h. The beads were then washed and resuspended in a wash buffer. The cell lysate was snap-chilled on ice, combined with the antibody-conjugated beads and rotated at 4 °C for 2 h. After placing the tube on a magnetic stand, the supernatant was discarded. The beads were washed multiple times with wash buffer, followed by washes with high-salt wash buffer and PNK buffer. Subsequent steps followed the same procedure as previously described.

ScRNA-seq

Primary mouse T cell suspensions were isolated from B16-OVA-bearing $Cas9^+$ B6 mice adoptively transferred with sgCtrl and sg*Larp4*-transduced C9OT-I T cells. $CD8^+$ single cells were sorted for library construction of scRNA-seq using Chromium Next GEM Single Cell 5′ Reagent Kit v2 (10× Genomics) according to the manufacturer's protocols. The libraries were sequenced on a DNBSEQ-T7 platform (MGI).

PRO-seq

PRO-seq was conducted as previously described[62]. T_N cells or $CD8^+$ T_{EX} cells (1×10^7) were permeabilized and subjected to a 5 min run-on reaction with biotin-11-CTP/UTP and ATP/GTP. RNAs were extracted, fragmented and biotin-labeled RNAs purified using streptavidin beads. Sequential 3′ and 5′ RNA adaptor ligations were performed on beads, followed by reverse transcription and 15 cycles of PCR amplification. Libraries (160–400 bp) were gel-purified and sequenced on an Illumina NovaSeq 6000.

RPLace-seq and RNA-seq data analysis

Quality control was performed by FastQC (v.0.11.8). The 4 bp unique molecular identifier (UMI) from Read1 was removed and appended to the read name by using UMI-tools (v.1.1.2)[63]. The adaptor and low-quality bases were trimmed by Trim Galore! (v.0.6.7) with the command 'trim_galore -q 20–length 10–stringency 3–phred33–paired'. The clean reads were first aligned to mouse rRNA sequences, and unmapped reads were aligned to the mouse(mm10) reference genome with STAR[64] using default parameters. Uniquely and concordantly aligned reads were then filtered by Sambamba (v.0.8.2)[65]. The PCR duplicates were removed using UMI-tools. Read1 was extracted by Sambamba, and counts in the CDS region (RPLace-seq) and exon regions (RNA-seq) were calculated by HOMER (v.4.11)[66] using the RefSeq select genomic annotation. Meta gene plots were created using the GenomicRanges (v.1.50.2)[67] R package. The RPF abundance (RPLace-seq), mRNA levels (RNA-seq) and TE (RPF/mRNA) of each sample were calculated by the regularized logarithm transformation (rlog) algorithm implemented in DESeq2. The mRNAs with significant differential TE were defined by a threshold of $P < 0.05$ and $|\log_2(\text{fold change})| > 0.5$. Genes with low translation, defined as genes having fewer than five counts in more than two RPLace-seq samples, were excluded from the analysis of detecting hypertranslated mRNAs. For analyzing the expression of LARP4-targeted mRNAs in Larp4-KO and control T_{EX} cells, housekeeping genes[68] were used for estimating the size factor. The mRNAs with significant differential TE were defined by a threshold of $P < 0.01$ and $|\log_2(\text{fold change})| > 0.5$. For comparing RPLace-seq and polysome profiling, the expression of RPLace-seq and polysome profiling was normalized using Rank-In[69]. Heatmaps were generated using the ComplexHeatmap (v.2.14.0)[70] R package.

LACE-seq data analysis

Quality control procedures were performed as described for the RPLace-seq analysis above. Clean reads were first aligned to mouse rRNA sequences and the first reads of the remaining unmapped paired-end reads were then aligned to the mouse (mm10) reference genome with Bowtie[71] with the parameter '-v 2 -m 10 -best -strata; -v 2 -k 10 -best -strata' as previously described[17]. Uniquely aligned reads were then filtered by Sambamba, and the PCR duplicates were removed using UMI-tools. To identify the LARP4-targeted sites, we performed a four-step analysis: (1) merged the aligned reads from three replicates into a single bam file using Sambamba; (2) called the truncation sites using PureCLIP (v.1.3.1)[72] with default parameters; (3) extended truncation sites by adding ~50–100 nucleotides 3′ downstream to obtain the extended region, determining the extension length at each site based on the highest normalized count difference (LARP4 versus IgG) from merge bam; and (4) calculated the adjusted signal enrichment score S for each extended region with equation (1):

$$S = \alpha \times \log FC\,(LARP4/IgG) \quad (1)$$

where logFC(LARP4/IgG) is calculated by diffBind (v.3.8.4)[73] using replicate samples between LARP4-IP and IgG-IP groups and α is the ratio of the current region length to the mRNA length, divided by the ratio of the average region length to the average mRNA length. All LARP4-targeted regions were determined by threshold $S \geq 3.5$.

scRNA-seq analysis

ScRNA-seq data were processed with Cell Ranger Single Cell Software Suite (v.6.0.2) and mapped to the mm10 reference genome.

Low-quality cells (expressing <200 or >7,000 genes or >10% mitochondrial genes) were filtered out. Gene counts in control and *Larp4*-KO cells were normalized by the sctransform algorithm, implemented in the Seurat R package (v.4.3.0)[74,75]. Cell cycle and mitochondrial/ribosome gene proportions were regressed out when scaling the variable features. The batch effect was removed by Harmony (v.0.1.1)[76]. One to ten Harmony-corrected PCs were then used for dimension reduction and unsupervised clustering. Clusters with high expression of melanoma or myeloid-related markers (*Pmel*, *Tyrp1*, *Itgam*) and low expression of T cell marker (*Cd3e*) were removed. The markers in each cluster were calculated based on the FindAllMarkers function in the Seurat package with default parameters. The gene set scores were calculated using the AddModuleScore function in the Seurat package, and the curated gene signatures are listed in Supplementary Table 5. Trajectory analysis was performed using diffusion maps in the Scanpy toolkit (v.1.9.6) using Harmony-corrected PCs[77].

PRO-seq analysis

The adaptor sequences from raw data of qPRO-seq were trimmed by Fastp (v.0.22.0)[78] for both R1 and R2 reads. Only reads with quality >Q20 were kept for downstream analyses. Reads from rRNAs were filtered by mouse reference genome (version mm10) using Bowtie2 (v.2.4.1)[79] with default parameters. The remaining reads were aligned using STAR with default parameters. The mapped reads were split into forward reads and reverse reads using SAMtools (v.1.6)[80]. BigWig files were generated using bamCoverage from deepTools based on BPM normalization in a 1 bp bin size.

Functional enrichment analysis

Functional enrichment analysis and gene set enrichment analysis were performed on mouse gene sets downloaded from the MSigDB database[21] by clusterProfiler (v.4.6.0)[81]. The gene set score of OXPHOS mRNAs across samples was calculated by gene set variation analysis implemented in the GSVA R package (v.1.46.0)[82].

Public data analysis

Pre-processed eCLIP-seq bed files were downloaded from the ENCODE database[23]. Peaks were filtered by $\log_2$(CLIP-IP/Input) > 4 and $-\log_{10}$(*P* value) > 7 and annotated using ChIPseeker (v.1.34.1)[83]. The filtered RBP-targeted mRNAs from K562 and HepG2 were merged. Human–mouse gene symbol mapping was obtained from BioMart[84]. Enrichment of hypertranslated mRNAs in RBP targets was assessed by Fisher's exact test using fisher.test in R.

Publicly available data (ATAC-seq[15,85], RNA-seq[40], scRNA-seq[24,25,86], CUT&Tag for H3K27ac[87], CHIP-seq for TOX[88], NR4A1[89], NFAT[90], IRF4[91], BATF[92], BCL-6[93]) were downloaded from the Gene Expression Omnibus database using the accession numbers provided in the Data availability section. ATAC-seq, CHIP-seq and CUT&Tag data were pre-processed with Trim Galore! and aligned to the reference genome using Bowtie. RNA-seq and scRNA-seq were processed with the methods mentioned above. The BigWig files were downloaded from the ChIP-Atlas[94]. The activity-by-contact model (v.1.1.2)[95] was used to predict the potential regulation network in intratumor T_{EX} cells based on ATAC-seq and H3K27ac signal intensity.

Quantification and statistical analysis

Statistical analysis was conducted using Prism (v.10.0) software (GraphPad). Comparisons between two groups were performed using two-tailed unpaired Student's *t*-tests or a Mann–Whitney *U*-test. Data are presented as mean ± s.e.m. All experiments were performed two to three times. Data collection was not randomized. Data collection and analysis were not performed blind to the conditions of the experiments. Unless major experimental errors occurred, all data were included in the analyses.

Reporting summary

Further information on research design is available in the Nature Portfolio Reporting Summary linked to this article.

Data availability

RPLace-seq, RNA-seq, LACE-seq, scRNA-seq and PRO-seq data have been deposited in the Genome Sequence Archive (GSA) repository under accession codes CRA019040 and CRA019813. RBP eCLIP-seq data were downloaded from the ENCODE database (https://www.encodeproject.org/eclip). The mapping relationship between human and mouse gene symbols was downloaded from BioMart (https://asia.ensembl.org/biomart/martview). Other public sequencing data used in this study are as follows: polysome profiling on $CD8^+$ T_N cells (GEO, GSE71643), ATAC-seq for TdLNs T_{PEX} cells (GEO, GSE180084), ATAC-seq for tumor T_{EX} cells (GEO, GSE122713), CUT&Tag for H3K27ac in tumor T_{EX} cells (GEO, GSE175437), CHIP-seq for TOX (GEO, GSE93953), CHIP-seq for NR4A1 (GEO, GSE266286), CHIP-seq for NFAT (GEO, GSE64407), CHIP-seq for IRF4 (GEO, GSE54191), CHIP-seq for BATF (GEO, GSE149796), CHIP-seq for BCL-6 (GEO, GSE182034), RNA-seq for intratumor wild-type and *Tox*-KO T cells (GEO, GSE126973), scRNA for intratumor wild-type and *Nr4a1/2*-KO T cells (GEO, GSE247641), scRNA for intratumor OT-I T cells (GEO, GSE218372) and scRNA for intratumor T cells in patients with melanoma (GEO, GSE159251). Source data are provided with this paper.

References

51. Liu, Y. et al. Tumors exploit FTO-mediated regulation of glycolytic metabolism to evade immune surveillance. *Cell Metab.* **33**, 1221–1233.e11 (2021).
52. Chen, Z. et al. In vivo $CD8^+$ T cell CRISPR screening reveals control by Fli1 in infection and cancer. *Cell* **184**, 1262–1280.e22 (2021).
53. Zhao, H. et al. Genome-wide fitness gene identification reveals Roquin as a potent suppressor of CD8 T cell expansion and anti-tumor immunity. *Cell Rep.* **37**, 110083 (2021).
54. Abdel-Hakeem, M. S. et al. Epigenetic scarring of exhausted T cells hinders memory differentiation upon eliminating chronic antigenic stimulation. *Nat. Immunol.* **22**, 1008–1019 (2021).
55. Zhang, X. et al. Depletion of BATF in CAR-T cells enhances antitumor activity by inducing resistance against exhaustion and formation of central memory cells. *Cancer Cell* **40**, 1407–1422.e7 (2022).
56. Liu, Y. et al. Chimeric STAR receptors using TCR machinery mediate robust responses against solid tumors. *Sci. Transl. Med.* **13**, eabb5191 (2021).
57. Wu, L. et al. Tumor aerobic glycolysis confers immune evasion through modulating sensitivity to T cell-mediated bystander killing via TNF-α. *Cell Metab.* **35**, 1580–1596.e9 (2023).
58. Mattijssen, S. et al. LARP4 mRNA codon-tRNA match contributes to LARP4 activity for ribosomal protein mRNA poly(A) tail length protection. *Elife* **6**, e28889 (2017).
59. van der Windt, G. J. W., Chang, C. H. & Pearce, E. L. Measuring bioenergetics in T cells using a Seahorse extracellular flux analyzer. *Curr. Protoc. Immunol.* **113**, 3.16B.1–3.16B.14 (2016).
60. Buck, M. D. et al. Mitochondrial dynamics controls T cell fate through metabolic programming. *Cell* **166**, 63–76 (2016).
61. Han, D. et al. Anti-tumour immunity controlled through mRNA m^6A methylation and YTHDF1 in dendritic cells. *Nature* **566**, 270–274 (2019).
62. Judd, J. et al. A rapid, sensitive, scalable method for Precision Run-On sequencing (PRO-seq). Preprint at https://doi.org/10.1101/2020.05.18.102277 (2020).
63. Smith, T., Heger, A. & Sudbery, I. UMI-tools: modeling sequencing errors in unique molecular identifiers to improve quantification accuracy. *Genome Res.* **27**, 491–499 (2017).

64. Dobin, A. et al. STAR: ultrafast universal RNA-seq aligner. *Bioinformatics* **29**, 15–21 (2013).
65. Tarasov, A., Vilella, A. J., Cuppen, E., Nijman, I. J. & Prins, P. Sambamba: fast processing of NGS alignment formats. *Bioinformatics* **31**, 2032–2034 (2015).
66. Heinz, S. et al. Simple combinations of lineage-determining transcription factors prime *cis*-regulatory elements required for macrophage and B cell identities. *Mol. Cell* **38**, 576–589 (2010).
67. Lawrence, M. et al. Software for computing and annotating genomic ranges. *PLoS Comput. Biol.* **9**, e1003118 (2013).
68. Hounkpe, B. W., Chenou, F., de Lima, F. & De Paula, E. V. HRT Atlas v1.0 database: redefining human and mouse housekeeping genes and candidate reference transcripts by mining massive RNA-seq datasets. *Nucleic Acids Res.* **49**, D947–D955 (2021).
69. Tang, K. et al. Rank-in: enabling integrative analysis across microarray and RNA-seq for cancer. *Nucleic Acids Res.* **49**, e99 (2021).
70. Gu, Z., Eils, R. & Schlesner, M. Complex heatmaps reveal patterns and correlations in multidimensional genomic data. *Bioinformatics* **32**, 2847–2849 (2016).
71. Langmead, B., Trapnell, C., Pop, M. & Salzberg, S. L. Ultrafast and memory-efficient alignment of short DNA sequences to the human genome. *Genome Biol.* **10**, R25 (2009).
72. Krakau, S., Richard, H. & Marsico, A. PureCLIP: capturing target-specific protein-RNA interaction footprints from single-nucleotide CLIP-seq data. *Genome Biol.* **18**, 240 (2017).
73. Ross-Innes, C. S. et al. Differential oestrogen receptor binding is associated with clinical outcome in breast cancer. *Nature* **481**, 389–393 (2012).
74. Hafemeister, C. & Satija, R. Normalization and variance stabilization of single-cell RNA-seq data using regularized negative binomial regression. *Genome Biol.* **20**, 296 (2019).
75. Hao, Y. et al. Integrated analysis of multimodal single-cell data. *Cell* **184**, 3573–3587.e29 (2021).
76. Korsunsky, I. et al. Fast, sensitive and accurate integration of single-cell data with Harmony. *Nat. Methods* **16**, 1289–1296 (2019).
77. Wolf, F. A., Angerer, P. & Theis, F. J. SCANPY: large-scale single-cell gene expression data analysis. *Genome Biol.* **19**, 15 (2018).
78. Chen, S., Zhou, Y., Chen, Y. & Gu, J. fastp: an ultra-fast all-in-one FASTQ preprocessor. *Bioinformatics* **34**, i884–i890 (2018).
79. Langmead, B. & Salzberg, S. L. Fast gapped-read alignment with Bowtie 2. *Nat. Methods* **9**, 357–359 (2012).
80. Danecek, P. et al. Twelve years of SAMtools and BCFtools. *Gigascience* **10**, giab008 (2021).
81. Wu, T. et al. clusterProfiler 4.0: a universal enrichment tool for interpreting omics data. *Innovation (Camb.)* **2**, 100141 (2021).
82. Hanzelmann, S., Castelo, R. & Guinney, J. GSVA: gene set variation analysis for microarray and RNA-seq data. *BMC Bioinformatics* **14**, 7 (2013).
83. Yu, G., Wang, L. G. & He, Q. Y. ChIPseeker: an R/Bioconductor package for ChIP peak annotation, comparison and visualization. *Bioinformatics* **31**, 2382–2383 (2015).
84. Smedley, D. et al. BioMart—biological queries made easy. *BMC Genomics* **10**, 22 (2009).
85. Huang, Q. et al. The primordial differentiation of tumor-specific memory $CD8^+$ T cells as bona fide responders to PD-1/PD-L1 blockade in draining lymph nodes. *Cell* **185**, 4049–4066.e25 (2022).
86. Srirat, T. et al. NR4a1/2 deletion promotes accumulation of $TCF1^+$ stem-like precursors of exhausted $CD8^+$ T cells in the tumor microenvironment. *Cell Rep.* **43**, 113898 (2024).
87. Ford, B. R. et al. Tumor microenvironmental signals reshape chromatin landscapes to limit the functional potential of exhausted T cells. *Sci. Immunol.* **7**, eabj9123 (2022).
88. Page, N. et al. Expression of the DNA-binding factor TOX promotes the encephalitogenic potential of microbe-induced autoreactive $CD8^+$ T cells. *Immunity* **48**, 937–950.e8 (2018).
89. Hao, J. et al. NR4A1 transcriptionally regulates the differentiation of stem-like $CD8^+$ T cells in the tumor microenvironment. *Cell Rep.* **43**, 114301 (2024).
90. Martinez, G. J. et al. The transcription factor NFAT promotes exhaustion of activated $CD8^+$ T cells. *Immunity* **42**, 265–278 (2015).
91. Kurachi, M. et al. The transcription factor BATF operates as an essential differentiation checkpoint in early effector $CD8^+$ T cells. *Nat. Immunol.* **15**, 373–383 (2014).
92. Chen, Y. et al. BATF regulates progenitor to cytolytic effector $CD8^+$ T cell transition during chronic viral infection. *Nat. Immunol.* **22**, 996–1007 (2021).
93. Sun, Q. et al. BCL6 promotes a stem-like $CD8^+$ T cell program in cancer via antagonizing BLIMP1. *Sci. Immunol.* **8**, eadh1306 (2023).
94. Zou, Z., Ohta, T. & Oki, S. ChIP-Atlas 3.0: a data-mining suite to explore chromosome architecture together with large-scale regulome data. *Nucleic Acids Res.* **52**, W45–W53 (2024).
95. Fulco, C. P. et al. Activity-by-contact model of enhancer–promoter regulation from thousands of CRISPR perturbations. *Nat. Genet.* **51**, 1664–1669 (2019).

Acknowledgements

We thank Y. Xue (Institute of Biophysics, Chinese Academy of Sciences) for assistance with the LACE-seq experiment. We are grateful to M. Peng (Tsinghua University) for the gift of the Cas9 transgenic mice. We thank D. Pan (Tsinghua University) for the gift of the pMYS-U6-GFP plasmid and M. Xu (National Institute of Biological Sciences) for the gift of the pMSCV plasmid. We are grateful to X. Lin (Tsinghua University) for providing the Raji-Luc cell line. We thank X. Yang (Shanghai Jiao Tong University) for assistance with CAR T cell-related experiments. We thank B. Liang and C. Jiao (Core Facility, Center of Biomedical Analysis, Tsinghua University) for technical support with confocal microscopy and Seahorse XF96. We thank Z. Chang in the Animal Facility, Tsinghua University, for animal care support. We thank J. Zhu for valuable advice and guidance on mitochondrial metabolism. This work was funded by the National Natural Science Foundation of China (NSFC) T2495272, Strategic Priority Research Program of the Chinese Academy of Sciences (XDB0570101), NSFC 32121001, 22293052, 32370644, National Key R&D Program of China (2024YFA1802102, 2024YFC3405901), Beijing Natural Science Foundation (L244023), the Key Research Program of Frontier Sciences, Chinese Academy of Sciences (ZDBS-LY-SM013), Next-Generation Bioinformatics Algorithms (XDA0460302) and CAS Youth Interdisciplinary Team.

Author contributions

M.M.X. and D.H. conceived the project and supervised the research. Y.L. performed in vitro and in vivo experiments and performed data analysis with the help of J.L. and J.Y. Library construction, in vitro T cell function assay and qPCR validation were performed by Y.L., J.Y., I.S., B.E.S., J.H. and S.L.; Z.Z. performed library construction of scRNA-seq. H.N. performed bioinformatics analysis. S.D.S., M.S.P. and M.K. provided support for T cell metabolism experiments. F.Z. analyzed the PRO-seq data. Y.Z., Z.H. and Y.X. proofread the paper. T.W.M. provided support and supervision during the paper revision process. M.M.X., D.H., H.N., Y.L. and J.L. wrote the paper with input from all authors. M.M.X. and D.H. acquired funding for the project. All authors discussed the results and commented on the paper. All authors approved the final draft and agreed to the submission for publication.

Competing interests
The authors declare no competing interests.

Additional information
Extended data is available for this paper at https://doi.org/10.1038/s41590-025-02232-5.

Supplementary information The online version contains supplementary material available at https://doi.org/10.1038/s41590-025-02232-5.

Correspondence and requests for materials should be addressed to Dali Han or Meng Michelle Xu.

Peer review information *Nature Immunology* thanks Ping-Chih Ho and the other, anonymous, reviewer(s) for their contribution to the peer review of this work. Primary Handling Editor: Nick Bernard, in collaboration with the *Nature Immunology* team.

https://doi.org/10.1038/s41590-025-02232-5

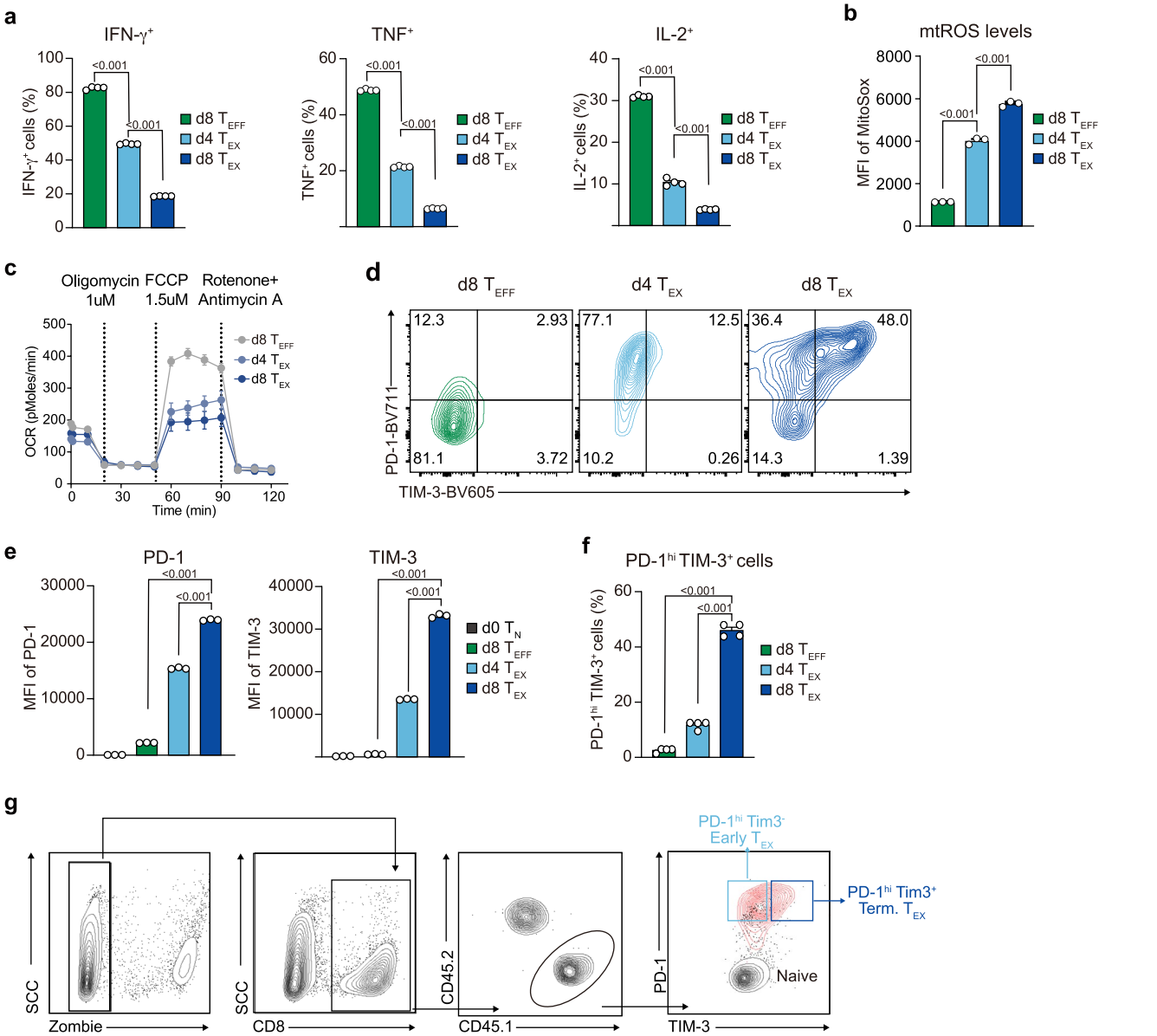

Extended Data Fig. 1 | Characterization of chronically stimulated T cell exhaustion phenotype. **(a)** Bar plots showing the percentage of cells expressing IFN-γ, TNF, or IL-2 in acutely stimulated d8 T_{EFF} cells, and chronically stimulated d4 and d8 T_{EX} cells ($n = 4$). **(b)** Bar plots showing the levels of mitochondrial reactive oxygen species (mtROS, measured using MitoSox) in d8 T_{EFF}, d4 $T_{EX,}$ and d8 T_{EX} cells ($n = 3$). **(c)** Oxygen consumption rate (OCR) using the Seahorse XF bioanalyzer measuring the respiratory capacity of d8 T_{EFF} cells, d4 T_{EX} cells, and d8 T_{EX} cells. Cells were seeded at 5 ×105/well in the XF96 plate ($n = 5$). **(d)** Representative flow cytometry analysis showing the expression of PD-1 and TIM-3 in d8 T_{EFF}, d4 $T_{EX,}$ and d8 T_{EX} cells. **(e)** Bar plots showing the MFI of PD-1 and TIM-3 in d0 T_N, d8 T_{EFF}, d4 $T_{EX,}$ and d8 T_{EX} cells ($n = 3$). **(f)** Bar plots showing the percentage of PD-1^{hi} TIM-3^+ $CD8^+$ T cells in d8 T_{EFF}, d4 $T_{EX,}$ and d8 T_{EX} cells ($n = 4$). **(g)** Flow cytometry gating strategy to identify PD-1^{hi} TIM-3^- early T_{EX} and PD-1^{hi} TIM-3^+ terminal T_{EX} in tumor-infiltrating OT-I T cells. *n*, number of technical replicates. For statistical analysis, figures (**a-c** and **e-f**) are presented as mean ± SEM and figures (**a-b** and **e-f**) were analyzed using unpaired two-sided Student's t-tests. The data represent three independent experiments (**a-c** and **e-f**).

https://doi.org/10.1038/s41590-025-02232-5

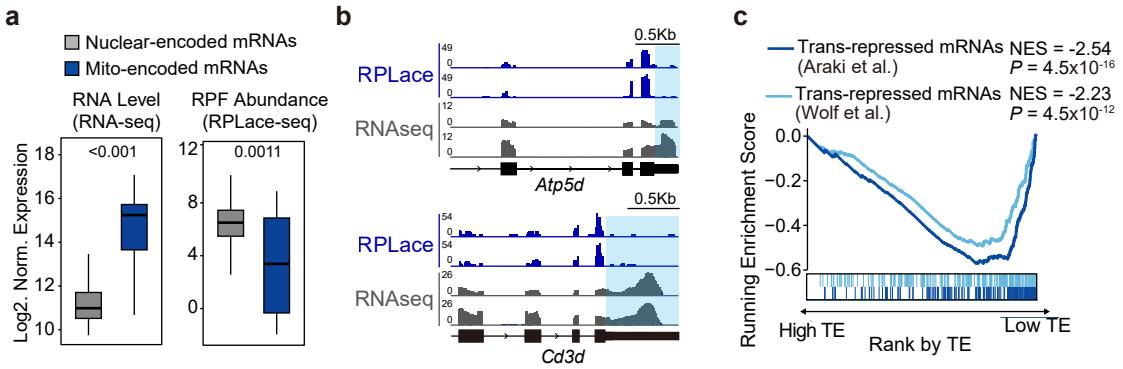

Extended Data Fig. 2 | Differential analysis of RPF and TE between d8 Tex and d4 Tex cells. (a) Boxplot showing the RNA level (left) and RPF abundance (right) of nuclear-encoded mRNAs ($n = 1314$, filtered lowly expressed mRNAs with RNA level < 10) and mitochondrial-encoded mRNAs ($n = 13$) in naïve CD8$^+$ T cells, as measured by RNA-seq and RPLace-seq. *P*-value was calculated with the two-sided Student's t-tests. **(b)** Representative IGV tracks showing read coverage of RPLace-seq and RNA-seq in the 3′UTR of *Atp5d* and *Cd3d* genes in naïve CD8$^+$ T cells. 3′UTR of genes were highlighted with blue background color. **(c)** GSEA to assess the enrichment of translation-repressed mRNAs in high-translating (high TE) mRNAs or low-translating (low TE) mRNAs in naïve CD8$^+$ T cells. Transcripts were ranked based on TE in naïve CD8$^+$ T cells. NES, normalized enrichment score. *P*-value was calculated with the two-sided permutation test.

https://doi.org/10.1038/s41590-025-02232-5

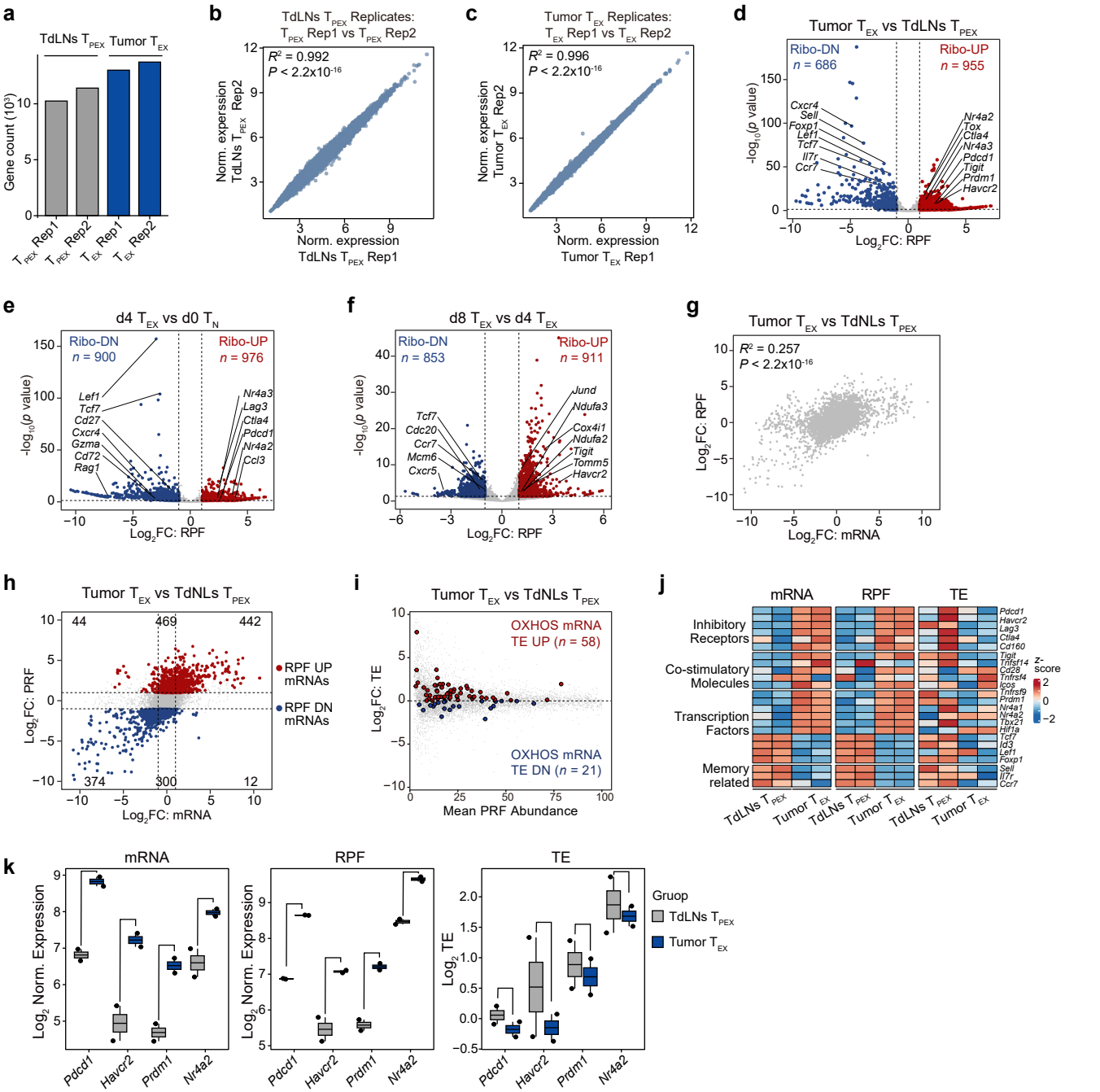

Extended Data Fig. 3 | Translatome landscapes of tumor-specific and *in vitro* chronically stimulated CD8⁺ T cells profiled by RPLace-seq. (a) Bar plot showing the gene count of mRNAs (TPM > 0.5) identified by RPLace-seq in TdLNs T_{PEX} and Tumor T_{EX} cells. **(b** and **c)** Scatter plot comparing normalized expression (rlog) of mRNAs between RPLace-seq replicates in TdLNs T_{PEX} cells **(b)** and Tumor T_{EX} cells **(c)**. Pearson correlation was used to assess agreement, and the coefficient of determination(R^2), *P*-values (two-sided), and the line of best fit are indicated. **(d)** Volcano plot showing the differential analysis of RPF abundance between TdLNs T_{PEX} and Tumor T_{EX} cells. Genes with significantly differential RPF abundance were defined by threshold $|\log_2FC| > 1$ and *P*-value < 0.05. *P*-values were calculated with the two-sided Wald test. Numbers of up- or down-regulated genes are indicated. **(e** and **f)** Volcano plot showing the differential analysis of RPF abundance between d4 T_{EX} and d0 T_N **(e)**, and between d8 T_{EX} and d4 T_{EX} **(f)**. Genes with significantly differential RPF abundance were defined by threshold $|\log_2FC| > 1$ and *P*-value < 0.05. *P*-values were calculated with the two-sided Wald test. Numbers of up- or down-regulated genes are indicated. **(g)** Scatter plot comparing $\log_2FC$ of mRNA levels and RPF abundance between Tumor T_{EX} cells and TdLNs T_{PEX} cells. Pearson correlation was used to assess agreement, and the coefficient of determination (R^2) and *p*-value (two-sided) are indicated. **(h)** Scatter plot comparing $\log_2FC$ of mRNA levels and RPF abundance between Tumor T_{EX} cells and TdLNs T_{PEX} cells. The genes with significantly differential RPF abundance were highlighted and are further divided into three groups based on the $\log_2FC$ of mRNA levels: (i) less than −0.5, (ii) between −0.5 and 0.5, or (iii) greater than 0.5. The mRNA numbers in each group are indicated. **(i)** Scatter plot showing the $\log_2FC$ of TE and mean RPF abundance in Tumor T_{EX} cells and TdLNs T_{PEX} cells. OXPHOS mRNAs are highlighted in red ($\log_2FC$ TE > 0) or blue ($\log_2FC$ TE < 0). The mRNA numbers in each group are indicated. **(j)** Heatmap showing the relative levels of mRNA, RPF, and TE across indicated gene sets in Tumor T_{EX} cells and TdLNs T_{PEX} cells. **(k)** Box plots showing the mRNA levels, RPF abundance, and TE for indicated genes in Tumor T_{EX} cells and TdLNs T_{PEX} cells ($n = 2$).

https://doi.org/10.1038/s41590-025-02232-5

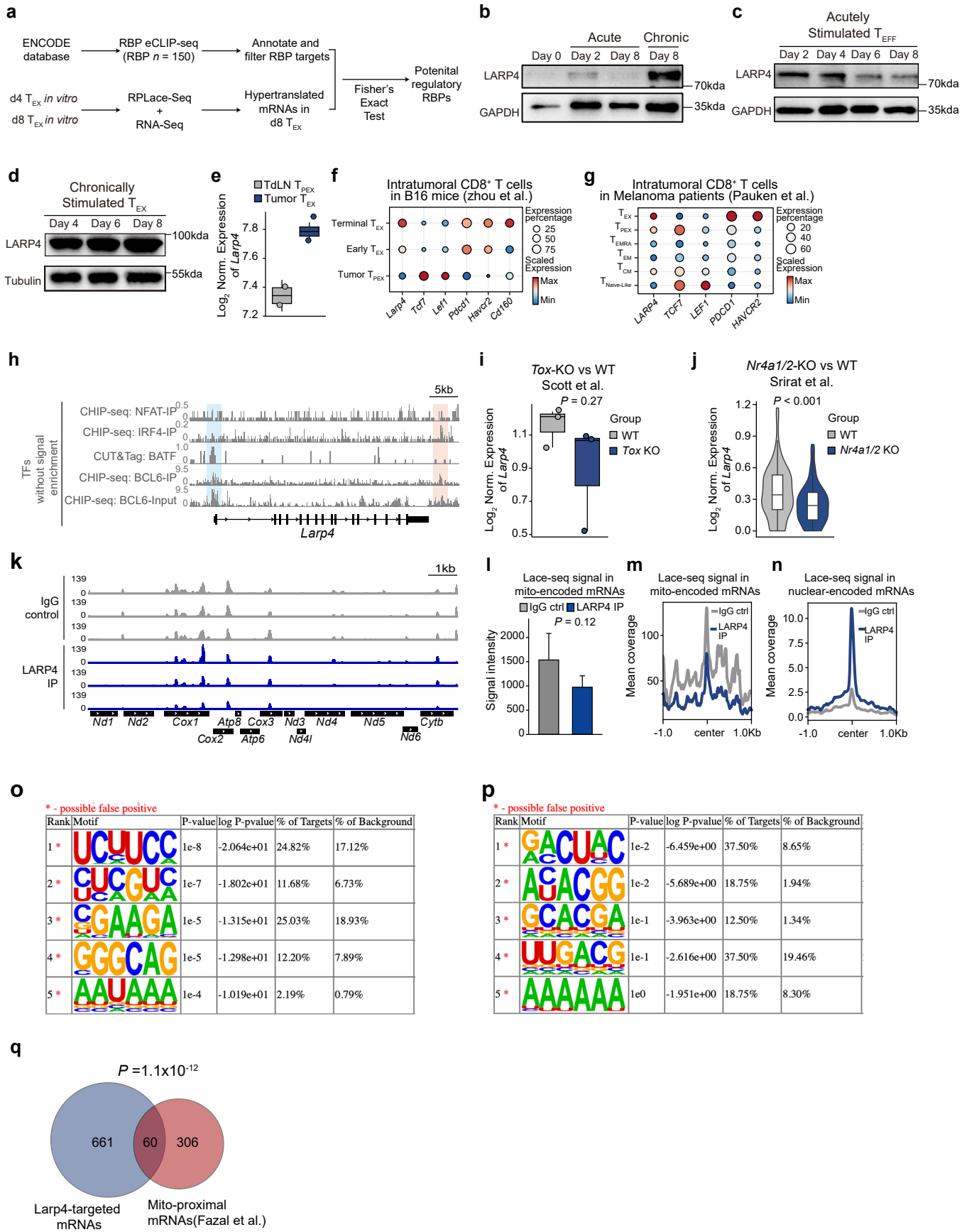

Extended Data Fig. 4 | See next page for caption.

https://doi.org/10.1038/s41590-025-02232-5

Extended Data Fig. 4 | LARP4 selectively targets hypertranslated mRNAs, particularly nuclear-encoded OXPHOS mRNAs, in exhausted CD8 + T cells. **(a)** Schematic diagram of workflow for searching the potential regulatory RBPs for hypertranslated mRNAs in d8 T_{EX} cells. **(b-d)** Immunoblotting of LARP4 in $CD8^+$ T_N cells, T_{EFF} cells, and T_{EX} cells under *in vitro* chronic or acute antigenic stimulation with indicated days. **(e)** Box plots showing the *Larp4* expression in Tumor T_{EX} cells and TdLNs T_{PEX} cells ($n = 2$). **(f)** Dot plots showing the *Larp4* expression in three subsets of tumor-infiltrating OT-I T cells in the B16-OVA mice model (GSE218372). **(g)** Dot plots showing the *LARP4* expression in six subsets of tumor-infiltrating $CD8^+$ T cells in patients with melanoma (GSE159251). **(h)** IGV tracks showing signal of translation factors without significant signal enrichment at *Larp4* loci and the nearby enhancer region, including NFAT (GSE64407), IRF4 (GSE54191), BATF (GSE149796), and BCL-6 (GSE182034). The promoter and enhancer regions are highlighted with a colored background. **(i)** Boxplot showing the Larp4 expression in WT and *Tox*-KO tumor-infiltrating $CD8^+$ T cells ($n = 3$) by RNA-seq (GSE126973). *P*-values were calculated using two-sided unpaired Student's t-tests. **(j)** Violin plot showing the Larp4 expression in WT and *Nr4a1/2*-KO tumor-infiltrating PD-1^+ TIM-3^+ $CD8^+$ T cells by scRNA-seq (GSE247641). Gene expression was normalized by sctransform algorithm and ten neighboring cells were merged into metacells. *P*-values were calculated using two-sided unpaired Student's t-tests. **(k)** IGV tracks showing the LACE-seq signal intensity for LARP4-IP and IgG control across mitochondrial-encoded RNA regions. **(l)** Bar plot showing the LACE-seq signal intensity of LARP4-IP and IgG control at reads-accumulated sites in mitochondrial-encoded RNA regions ($n = 39$). The reads-accumulated sites were identified by peak calling using LARP4-IP data alone. The diffBind was used to quantify signal intensity in LARP4-IP and IgG control at these sites. *P* value is calculated by two-sided unpaired Student's t-tests. **(m)** Profile plot showing the LACE-seq signal intensity for LARP4-IP and IgG control at reads-accumulated sites in mitochondrial-encoded mRNA regions. The deeptools was used to quantify coverage differences between LARP4-IP and IgG control at these sites. **(n)** Profile plot showing the LACE-seq signal intensity for LARP4-IP and IgG control at LARP4-targeted sites in nuclear-encoded mRNA regions. **(o** and **p)** Top 5 motifs identified by HOMER across total LARP4-targeted sites **(o)** and on LARP4-targeted sites within OXPHOS mRNAs **(p)** in T_{EX} cells after 8 days of *in vitro* antigenic stimulation. The asterisk (*) indicates the non-significant motif as labeled by HOMER. **(q)** Venn diagram showing the overlap between LARP4-targeted mRNAs and mitochondria-proximal mRNAs identified by APEX-seq (Fazal et al). *P*-value is calculated by one-sided Fisher's exact test. The data represent three independent experiments (**b-d**).

https://doi.org/10.1038/s41590-025-02232-5

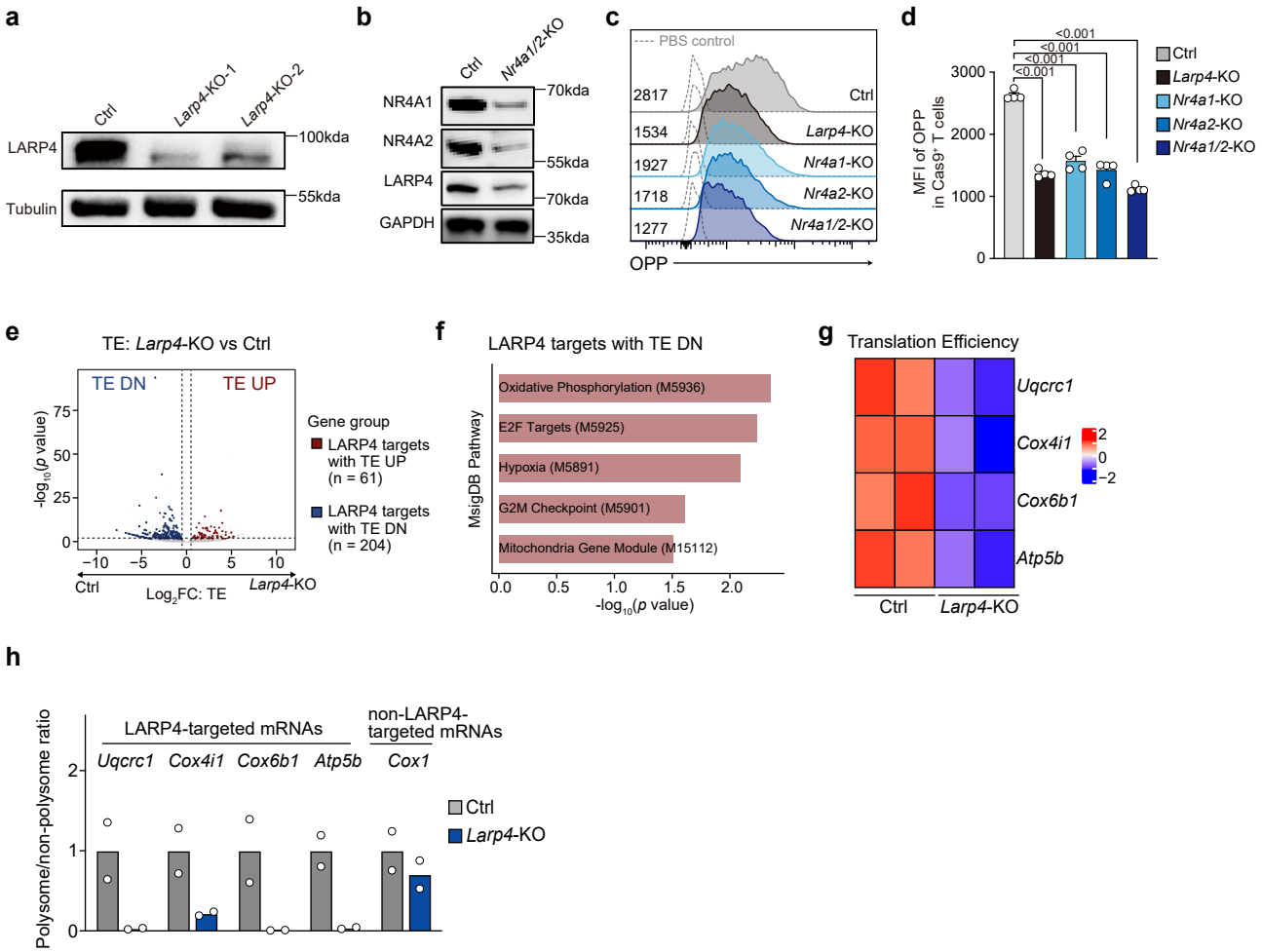

Extended Data Fig. 5 | LARP4 is regulated by NR4A1/2 and modulate mRNA translation in exhausted CD8$^+$ T cells. (a) Immunoblotting is shown to validate changes in LARP4 expression in control and *Larp4*-KO T_{EX} cells after 8 days of *in vitro* chronic antigenic stimulation. **(b)** Immunoblotting showing the change of LARP4 expression in control and *Nr4a1/2*-KO Cas9$^+$ T cells after 6 days of *in vitro* chronic antigenic stimulation. **(c** and **d)** Representative flow cytometry histograms **(c)** and bar plots **(d)** showing OPP incorporation in control, *Larp4*-KO, *Nr4a1*-KO, *Nr4a2*-KO and *Nr4a1/2*-KO Cas9$^+$ T cells after 6 days of chronic antigenic stimulation ($n = 4$). *P*-values were calculated using two-sided unpaired Student's t-tests. Data are shown as mean ± SEM. **(e)** Volcano plot showing mRNAs with differential TE between control and *Larp4*-KO T_{EX} cells. LARP4-targeted mRNAs with significant differential TE ($|\log_2 FC| > 0.5$, p-value < 0.01) are highlighted. **(f)** MSigDB pathway analysis of LARP4-targeted mRNAs with significantly downregulated TE after *Larp4* knockout. The systematic name of each pathway in MSigDB is labeled. **(g)** Heatmap showing the TE of indicated genes in control and *Larp4*-KO in exhausted T cells after 8 days of *in vitro* chronic antigenic stimulation. **(h)** Bar plot showing the polysome / non-polysome ratio of indicated LARP4-targeted mRNAs and non-LARP4-targeted mRNA revealed by sucrose polysome profiling and qPCR ($n = 2$). The data represent two independent experiments (**b, c, h**) and three independent experiments (**a**).

https://doi.org/10.1038/s41590-025-02232-5

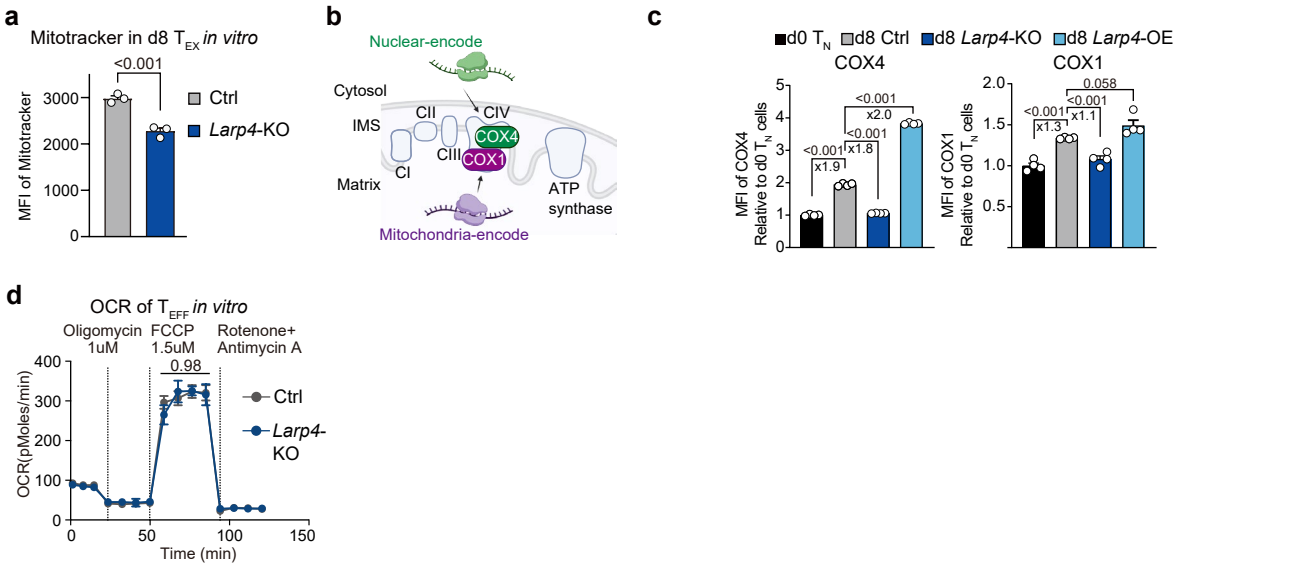

Extended Data Fig. 6 | LARP4 drives mitochondrial dysfunction in tumor-specific CD8$^+$ T cells. (a) Bar plots showing the levels of mitochondrial mass (measured by Mitotracker) in chronically stimulated d8 T_{EX} cells from control ($n = 3$) and *Larp4*-KO ($n = 3$) groups, represented as the MFI of Mitotracker staining. **(b)** Schematic diagram of the dual-genome-encoded mitochondrial electron transport complex showing nuclear-encoded COX4 (green) and mitochondrial-encoded COX1 (purple) components.CI–CV, Complexes I–V; IMS, intermembrane space. **(c)** Bar graphs showing the MFI of COX4 (left) and COX1 (right) proteins in the indicated group of T cells ($n = 4$). The expression levels of COX proteins were measured using flow cytometry and normalized to the levels in d0 T_N cells. **(d)** Oxygen consumption rate (OCR) using the Seahorse XF bioanalyzer measuring the respiratory capacity of control and *Larp4*-KO T_{EFF} cells after 6 days of *in vitro* acute antigenic stimulation. Cells were seeded at 5×10^5/well in the XF96 plate ($n = 6$). *n*, number of technical replicates. Data in plots of (**a, c, d**) are presented as mean ± SEM. Unpaired two-sided Student's t-tests were performed. The data represent two independent experiments in (**a, c, d**).

https://doi.org/10.1038/s41590-025-02232-5

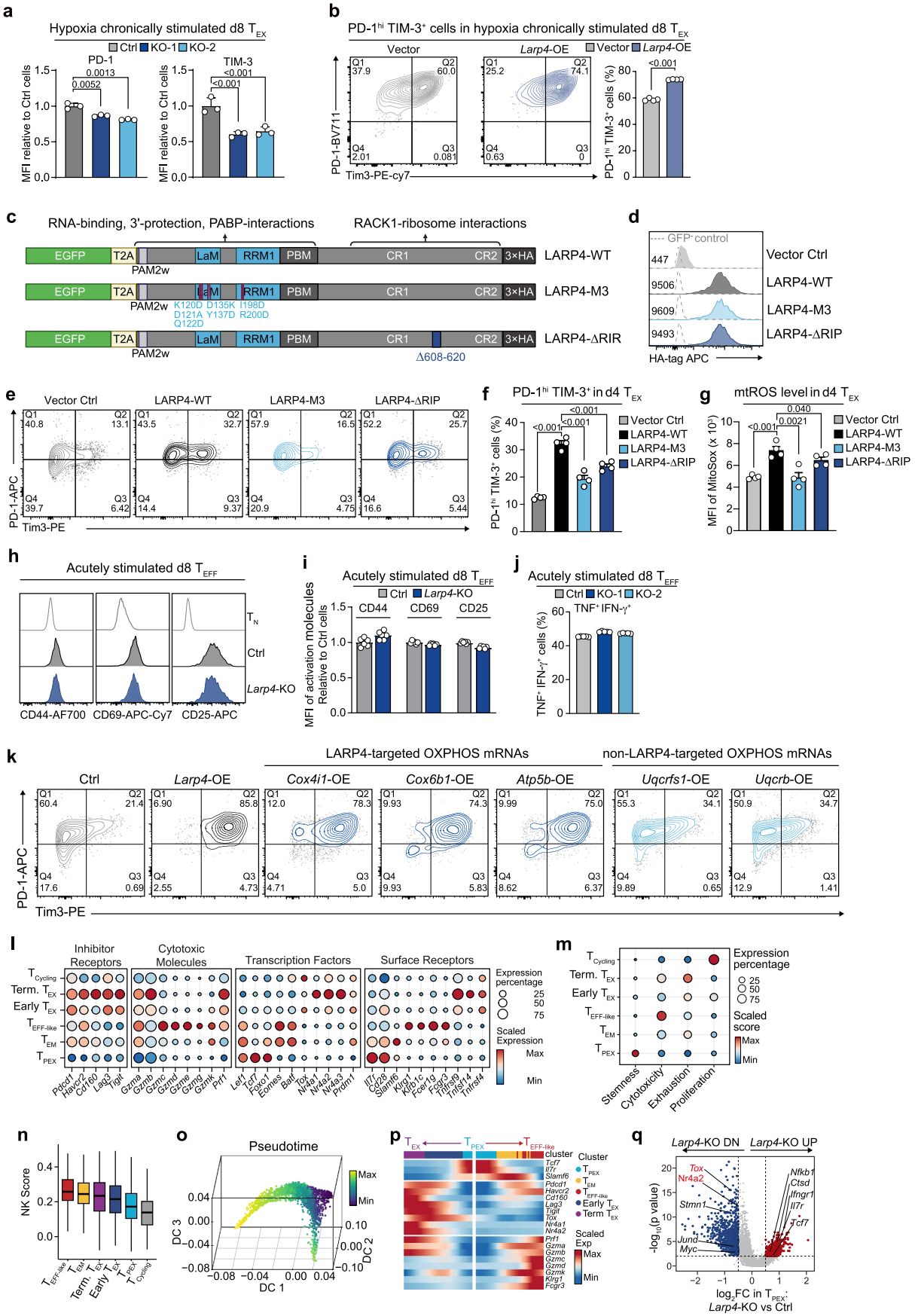

Extended Data Fig. 7 | See next page for caption.

https://doi.org/10.1038/s41590-025-02232-5

Extended Data Fig. 7 | The impact of *Larp4*-KO on T cell exhaustion and function *in vitro* and *in vivo*. **(a)** Bar plots showing the MFI of exhaustion markers PD-1 and TIM-3 in control and *Larp4*-KO T_{EX} cells after 8 days of *in vitro* chronic antigenic stimulation under hypoxia condition. The MFI values were normalized to control cells ($n = 3$). **(b)** Representative flow cytometry graphs and bar plots showing the percentage of PD-1^{hi} TIM-3^{+} cells in vector control and *Larp4*-overexpression (OE) T_{EX} cells after 8 days of *in vitro* chronic antigenic stimulation under hypoxia condition ($n = 4$). **(c)** Schematic diagram depicting the wild-type and mutant LARP4 constructs used in the experiment. The diagram illustrates the structural organization of the LARP4 protein, including the La motif (LaM), RNA recognition motif (RRM), conserved region-2 (CR2) and other relevant domains. Key mutations introduced in the LARP4-M3 and LARP4-ΔRIR constructs are highlighted, along with their positions relative to the conserved regions. **(d)** Representative flow cytometry histograms showing the expression of HA-tag in T cells overexpressing empty vector (Vector Ctrl), LARP4-WT, LARP4-M3 and LARP4-ΔRIR after 4 days of *in vitro* chronic antigenic stimulation. **(e** and **f)** Representative flow cytometry histograms **(e)** and bar plots **(f)** showing the percentage of PD-1^{hi} TIM-3^{+} cells in T cells overexpressing empty vector (Vector Ctrl), LARP4-WT, LARP4-M3 and LARP4-ΔRIR after 4 days of *in vitro* chronic antigenic stimulation ($n = 4$). **(g)** Bar plots showing the level of mtROS in T cells overexpressing empty vector (Vector Ctrl), LARP4-WT, LARP4-M3 and LARP4-ΔRIR after 4 days of *in vitro* chronic antigenic stimulation ($n = 4$), represented as the MFI of MitoSox staining. **(h)** Representative flow cytometry histograms showing the expression of activation markers CD44, CD69, and CD25 in T_N cells, control T_{EFF} cells, and *Larp4*-KO T_{EFF} cells after 8 days of *in vitro* acute antigenic stimulation. **(i)** Bar graphs showing the MFI of CD44, CD69, and CD25 activation markers in control and *Larp4*-KO T_{EFF} cells after 8 days of *in vitro* acute antigenic stimulation. The MFI values were normalized to control cells ($n = 6$). **(j)** Bar graphs showing the percentage of TNF^{+} IFN-γ^{+} cells in control and *Larp4*-KO T_{EFF} cells after 8 days of *in vitro* acute antigenic stimulation ($n = 5$). **(k)** Representative flow cytometry graphs showing the percentage of PD-1^{hi} TIM-3^{+} cells in cells overexpressing empty vector (Ctrl), *Larp4*, indicated LARP4-targeted OXPHOS mRNAs and indicated non-LARP4-targeted mRNAs after 6 days of *in vitro* chronic antigenic stimulation. **(l)** Bubble heatmap depicting the expression of representative genes in each C9OT-I T cell subset. **(m)** Bubble heatmap depicting the gene set score of indicated signatures in each C9OT-I T cell subset. **(n)** Boxplot showing the gene set score of NK signatures in each C9OT-I T cell subset. **(o)** Pseudotime of trajectory in space of diffusion map. **(p)** Heatmap showing the transcriptional trends of indicated genes along the pseudotime in two differentiation trajectories. Color represents scaled expression levels. **(q)** Volcano plot showing mRNAs with differential expression between cells in control and *Larp4*-KO T_{PEX} subsets. mRNAs with significant differential expression ($|\log_2 FC| > 0.5$, *P*-value < 0.01) are highlighted. *n*, number of technical replicates (**a, b, f, g, h, i, j**). For statistical analysis, data in bar plots (**a, b, f, g, i, j**) are presented as mean ± SEM and unpaired two-sided Student's t-tests were performed for (**a, b, f**) and unpaired one-sided Student's t-tests were performed for (**g**). Boxplots in (**n**) include the following elements: center line, median; box limits, upper and lower quartiles; whiskers, 1.5 IQR of the upper quartile and lower quartile. The data represent two independent experiments (**a, b, f, g, i, j**).

https://doi.org/10.1038/s41590-025-02232-5

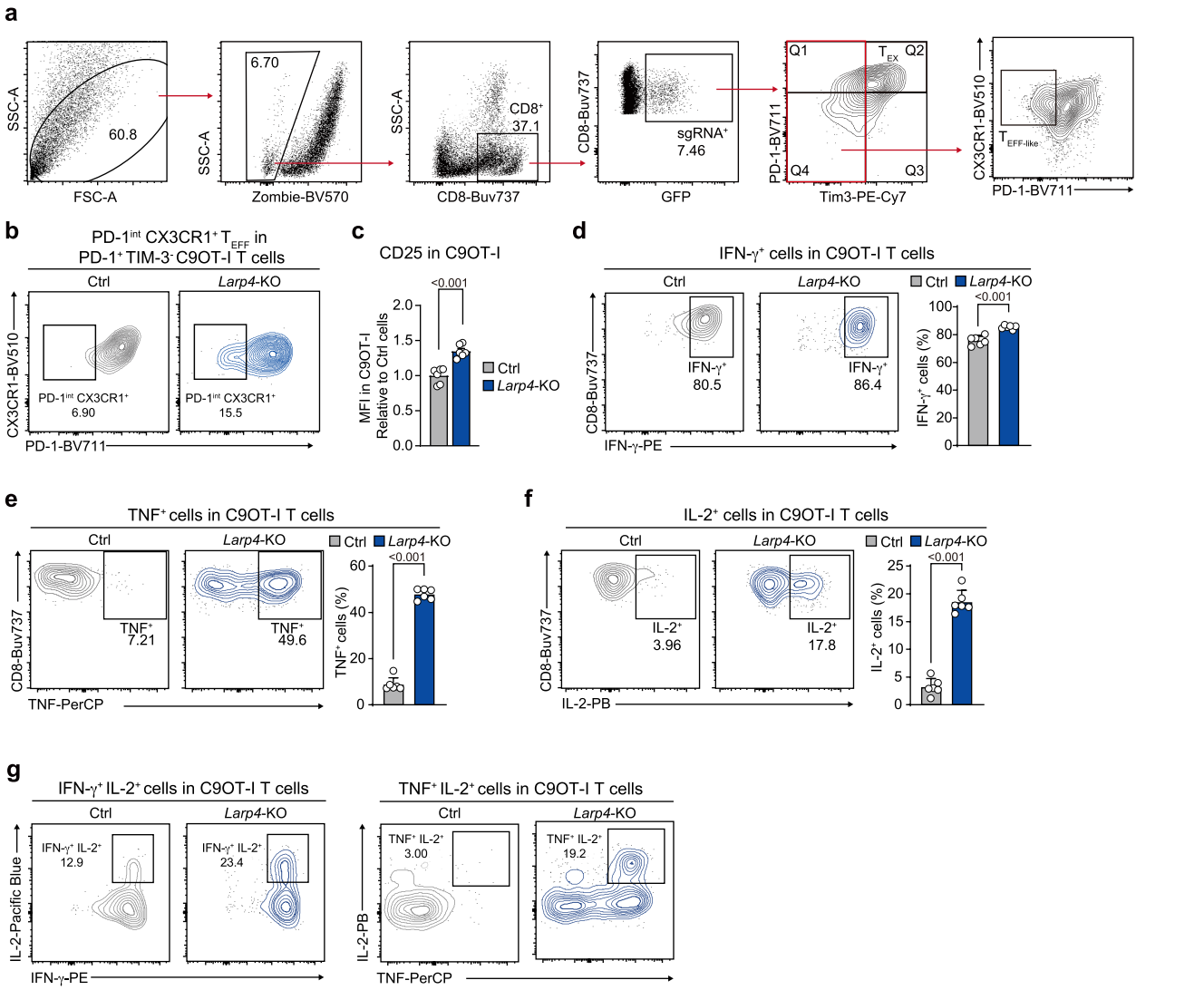

Extended Data Fig. 8 | Flow cytometry uncovers the impact of *Larp4*-KO on differentiation and function of tumor-specific CD8$^+$ T cell within TME. (a) Flow cytometry gating strategy to identify PD-1^{hi} TIM-3$^+$ T_{EX} cells and PD-1^{Int} CX3CR1$^+$ $T_{EFF\text{-}like}$ cells within TME. Endogenous cells were shown. **(b)** Representative flow cytometry graphs showing the percentage of PD-1^{int} CX3CR1$^+$ $T_{EFF\text{-}like}$ cells in control and *Larp4*-KO C9OT-I T cells within TME. PD-1^{int} CX3CR1$^+$ $T_{EFF\text{-}like}$ cells were gated from PD-1$^+$ TIM-3$^-$ C9OT-I T cells. **(c)** Bar plots showing the MFI of CD25 in control and *Larp4*-KO C9OT-I T cells within TME. The MFI values were normalized to control cells ($n = 6$). **(d)** Representative flow cytometry graphs and bar plots showing the percentage of IFN-γ$^+$ cells in control and *Larp4*-KO C9OT-I T cells within TME ($n = 6$). **(e)** Representative flow cytometry graphs and bar plots showing the percentage of TNF$^+$ cells in control and *Larp4*-KO C9OT-I T cells within TME ($n = 6$). **(f)** Representative flow cytometry graphs and bar plots showing the percentage of IL-2$^+$ cells in control and *Larp4*-KO C9OT-I T cells within TME ($n = 6$). **(g)** Flow cytometry graphs showing the percentage of IFN-γ$^+$ IL-2$^+$ (left) and TNF$^+$ IL-2$^+$ (right) cells in control and *Larp4*-KO C9OT-I T cells within TME. n, numbers of mice (**c**-**f**). For statistical analysis, data in bar plots are presented as mean ± SEM and unpaired two-sided Student's t-tests were performed for (**b**-**f**).

https://doi.org/10.1038/s41590-025-02232-5

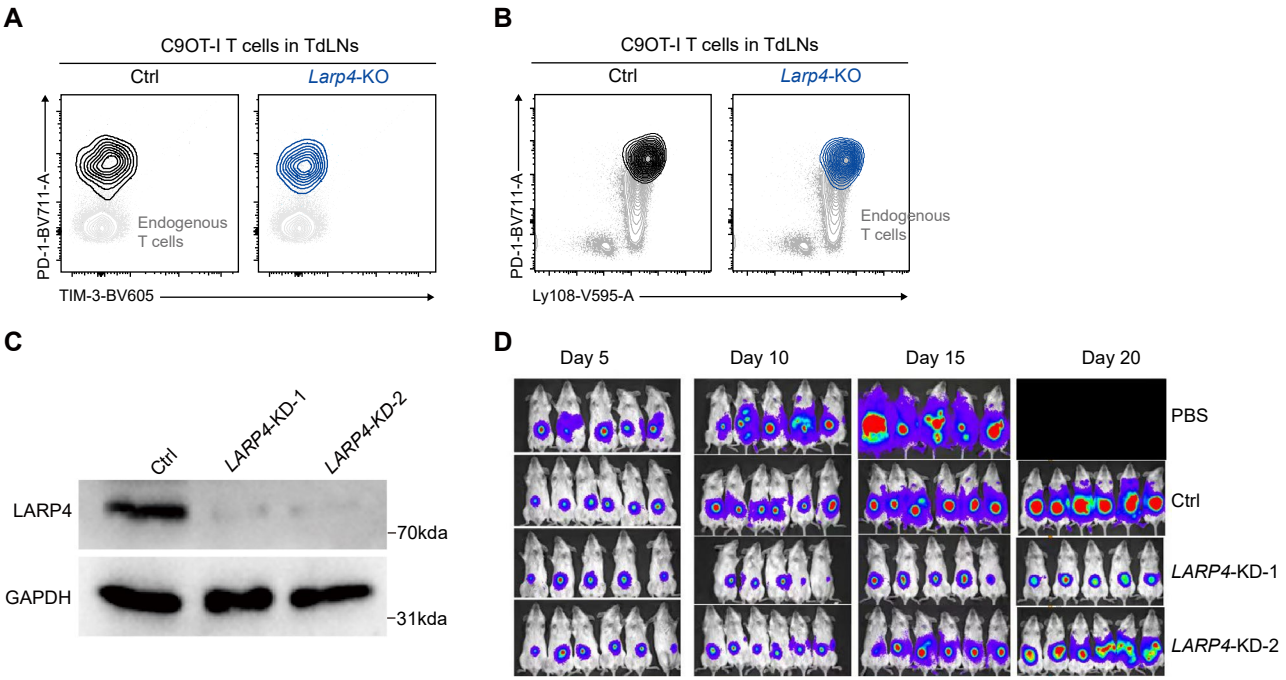

Extended Data Fig. 9 | Anti-tumor response of *LARP4*-KD CD20-CAR T cells. **(a)** Flow cytometry graphs showing the expression of PD-1 and TIM-3 in control and *Larp4*-KO C9OT-I T_{PEX} cells in TdLNs. Endogenous cells are shown in gray. **(b)** Flow cytometry graphs showing the expression of PD-1 and Ly108 in control and *Larp4*-KO C9OT-I T_{PEX} cells in TdLNs. Endogenous cells are shown in gray. **(c)** Western blot showing the expression of LARP4 and GAPDH in control and *LARP4*-KD CD20-CAR T cells. **(d)** Representative bioluminescence imaging of tumor-bearing mice treated with PBS, control CD20-CAR T cells, and *LARP4*-KD CD20-CAR T cells on days 5, 10, 15, and 20 post-tumor inoculation. These data represent two independent experiments.

nature portfolio

Corresponding author(s): Meng Michelle Xu

Last updated by author(s): Jun 5, 2025

Reporting Summary

Nature Portfolio wishes to improve the reproducibility of the work that we publish. This form provides structure for consistency and transparency in reporting. For further information on Nature Portfolio policies, see our Editorial Policies and the Editorial Policy Checklist.

Statistics

For all statistical analyses, confirm that the following items are present in the figure legend, table legend, main text, or Methods section.

n/a	Confirmed	
☐	☒	The exact sample size (*n*) for each experimental group/condition, given as a discrete number and unit of measurement
☐	☒	A statement on whether measurements were taken from distinct samples or whether the same sample was measured repeatedly
☐	☒	The statistical test(s) used AND whether they are one- or two-sided *Only common tests should be described solely by name; describe more complex techniques in the Methods section.*
☒	☐	A description of all covariates tested
☒	☐	A description of any assumptions or corrections, such as tests of normality and adjustment for multiple comparisons
☐	☒	A full description of the statistical parameters including central tendency (e.g. means) or other basic estimates (e.g. regression coefficient) AND variation (e.g. standard deviation) or associated estimates of uncertainty (e.g. confidence intervals)
☐	☒	For null hypothesis testing, the test statistic (e.g. *F*, *t*, *r*) with confidence intervals, effect sizes, degrees of freedom and *P* value noted *Give P values as exact values whenever suitable.*
☒	☐	For Bayesian analysis, information on the choice of priors and Markov chain Monte Carlo settings
☒	☐	For hierarchical and complex designs, identification of the appropriate level for tests and full reporting of outcomes
☐	☒	Estimates of effect sizes (e.g. Cohen's *d*, Pearson's *r*), indicating how they were calculated

Our web collection on statistics for biologists contains articles on many of the points above.

Software and code

Policy information about availability of computer code

Data collection	BD FACSDiva v8.0, Illumina NovaSeq 6000,
Data analysis	Details in methods, along with versions of specific software packages that were used. The following open source software packages were used in data analysis, as described in methods section: FastQC (v0.11.8), UMI-tools (v1.1.2), Trim Galore! (v0.6.7), STAR (v2.7.10a), sambamba (v0.8.2), HOMER (v4.11), GenomicRanges (v1.50.2), DESeq2 (v1.38.3), bowtie (v2.4.1 & v1.0.0), clusterProfiler (v4.6.0), deepTools (v3.5.1), Integrative Genomics Viewer (IGV v2.13.2), PureCLIP (v1.3.1), diffBind (v3.8.4), Cell Ranger Single-Cell Software Suit (v6.0.2), Seurat (v4.3.0), harmony (v0.1.1), Scanpy (v1.9.6), Fastp (v0.22.0), Bowtie2 (v2.4.1), SAMtools (v1.6), Rank-In (2021.8.27), ComplexHeatmap (v2.14.0), GSVA(v1.46.0), ChIPseeker (v1.34.1), Activity-by-Contact model (v1.1.2), FlowJo (V10), GraphPad Prism (v10).

For manuscripts utilizing custom algorithms or software that are central to the research but not yet described in published literature, software must be made available to editors and reviewers. We strongly encourage code deposition in a community repository (e.g. GitHub). See the Nature Portfolio guidelines for submitting code & software for further information.

Data

Policy information about availability of data

All manuscripts must include a data availability statement. This statement should provide the following information, where applicable:

- Accession codes, unique identifiers, or web links for publicly available datasets
- A description of any restrictions on data availability
- For clinical datasets or third party data, please ensure that the statement adheres to our policy

The sequencing data of RPLace-seq, RNA-seq, LACE-seq, scRNA-seq and PRO-seq have been deposited in the Genome Sequence Archive (GSA) repository with the accession number CRA019040 and CRA019813. RBP eCLIP-seq data was download fron the ENCODE database(https://www.encodeproject.org/eclip/). The mapping relationship between human and mouse Gene Symbols was downloaded from the BioMart (https://asia.ensembl.org/biomart/martview/). The accession number of other public sequencing data used in this study: Polysome Profiling on CD8+ naïve T cell (GEO: GSE71643), ATAC-seq for TdLNs TPEX cells (GEO: GSE180084), ATAC-seq for Tumor TEX cells (GEO: GSE122713), CUT&Tag for H3K27ac in Tumor TEX cells (GEO: GSE175437), CHIP-seq for TOX (GEO: GSE93953), CHIP-seq for NR4A1 (GEO: GSE266286), CHIP-seq for NFAT (GEO: GSE64407), CHIP-seq for IRF4 (GEO: GSE54191), CHIP-seq for BATF (GEO: GSE149796), CHIP-seq for BCL-6 (GEO: GSE182034), RNA-seq for intratumor WT and Tox-KO T cells (GEO: GSE126973), scRNA for intratumor WT and Nr4a1/2-KO T cells (GEO: GSE247641), scRNA for intratumor OT-I T cells (GEO: GSE218372), scRNA for intratumor T cells in patients with melanoma (GEO: GSE159251).

Research involving human participants, their data, or biological material

Policy information about studies with human participants or human data. See also policy information about sex, gender (identity/presentation), and sexual orientation and race, ethnicity and racism.

Reporting on sex and gender	N/A
Reporting on race, ethnicity, or other socially relevant groupings	N/A
Population characteristics	N/A
Recruitment	N/A
Ethics oversight	N/A

Note that full information on the approval of the study protocol must also be provided in the manuscript.

Field-specific reporting

Please select the one below that is the best fit for your research. If you are not sure, read the appropriate sections before making your selection.

☒ Life sciences ☐ Behavioural & social sciences ☐ Ecological, evolutionary & environmental sciences

For a reference copy of the document with all sections, see nature.com/documents/nr-reporting-summary-flat.pdf

Life sciences study design

All studies must disclose on these points even when the disclosure is negative.

Sample size	According to the 3R policy (replacement, reduction, and refinement) of our institution, the minimum number of mice necessary for the statistical significance were used. The sample size was chosen empiricaly, 3-8 mice per group is usually enough to achieve statistical significance. In some experiments with big variations, more animals (more biological repeats) are pooled to reach statistical significance. For experiments other than mice, sample sizes were chosen based on commonly accepted standards in the field and by referencing previously published studies with similar experimental designs. Liu et al. (Tumors exploit FTO-mediated regulation of glycolytic metabolism to evade immune surveillance, Cell metabolism, 2021)
Data exclusions	No data were excluded in this study.
Replication	The number of replicates were indicated in the figure legends.
Randomization	Co-housed littermates were randomly assigned to each group for comparison. For experiments other than mice (e.g., in vitro assays, flow cytometry, sequencing), samples were allocated based on predefined biological conditions (such as Knockout vs. control groups).All samples were processed simultaneously using standardized protocols, and relevant covariates were carefully controlled or balanced across groups to ensure comparability between experimental groups.
Blinding	Animal numbers (n) rather than genotypes were used during experimental procedures to achieve Blinding. In addition, there was no subjective measurement in the experimental procedures.

Reporting for specific materials, systems and methods

We require information from authors about some types of materials, experimental systems and methods used in many studies. Here, indicate whether each material, system or method listed is relevant to your study. If you are not sure if a list item applies to your research, read the appropriate section before selecting a response.

Materials & experimental systems

n/a	Involved in the study
☐	☒ Antibodies
☐	☒ Eukaryotic cell lines
☒	☐ Palaeontology and archaeology
☐	☒ Animals and other organisms
☒	☐ Clinical data
☒	☐ Dual use research of concern
☒	☐ Plants

Methods

n/a	Involved in the study
☒	☐ ChIP-seq
☐	☒ Flow cytometry
☒	☐ MRI-based neuroimaging

Antibodies

Antibodies used

Antibodies used for flow cytometry are:
Anti-CD4, BioLegend, Cat#100414; RRID: AB_312699 (1:500)
Anti-CD8, Biolegend, Cat#100712; RRID: AB_312751 (1:500)
Anti-CD8a, Abcam, Cat#ab22504; RRID: AB_447109 (1:500)
Anti-CD45.1, BioLegend, Cat# 101216; RRID: AB_312799 (1:500)
anti-CD45.2, BioLegend, Cat# 109806; RRID: AB_313443 (1:500)
anti-PD-1, BioLegend, Cat# 135231; RRID: AB_2566158 (1:500)
anti-TIM-3, BioLegend, Cat# 119721; RRID: AB_2616907 (1:500)
anti-Ly108, BioLegend, Cat# 134608; RRID: AB_2188093 (1:500)
anti-CX3CR1, BioLegend, Cat# 149035; RRID: AB_2629605 (1:500)
anti-CD39, eBioscience, Cat# 25-0391-82; RRID: AB_1210502 (1:500)
anti-TIGIT, eBioscience, Cat# 12-9501-80; RRID: AB_2866364 (1:500)
Anti-CD69, BioLegend, Cat#104522; RRID: AB_2260065 (1:500)
Anti-Granzyme B, BioLegend, Cat#372206; RRID: AB_2687030 (1:500)
Anti-IFN-g, BioLegend, Cat#505808; RRID: AB_315402 (1:500)
Anti-HA-probe (Y-11), Santa Cruz Biotechnology, Cat# sc-805; RRID: AB_631618 (1:500)
Goat Anti-Rabbit IgG H&L (Alexa Fluor 488) , Abclonal, Cat# ab150077; RRID: AB_2630356 (1:2000)
The following Abs were used for western blot:
Anti-a-Tubulin, Proteintech, Cat#66031-1-Ig; RRID: AB_11042766 (1:10000)
Anti-a-Actin-HRP, Santa Cruz Biotechnology, Cat#sc-47778; RRID: AB_2714189 (1:10000)
Anti-LARP4, Proteintech, Cat#16529-1-AP; RRID: AB_2296671 (1:500)
Anti-NDUFB8, Proteintech, Cat# 14794-1-AP; RRID: AB_2150970 (1:1000)
Anti-SDHB, Proteintech, Cat# 10620-1-AP; RRID: AB_2285522 :(1:1000)
Anti-UQCRC2, Abclonal, Cat A4181#; RRID: AB_2765543 (1:1000)
Anti-ATP5A1, Abclonal, Cat A5884#; RRID: AB_2766632 (1:500)
Anti- ND1, Abclonal, Cat# A5250; RRID: AB_2766080 (1:1000)
Anti- ND5, Abclonal, Cat# A12465; RRID: AB_2759309 (1:1000)
Anti-ATP6, Abclonal, Cat# A8193; RRID: AB_2768510 (1:500)
HRP-conjugated goat anti-rabbit IgG, Cwbio, Cat#CW0103; RRID: AB_2814709 (1:10000)
HRP-conjugated goat anti-mouse IgG, Cwbio, Cat#CW0102; RRID: AB_2814710 (1:10000)
HRP-conjugated goat anti-rat IgG, Santa Cruz Biotechnology, Cat#sc-2032, RRID: AB_631755 (1:10000)
Anti-UQCRC1, Thermo Fisher Scientific, Cat#459140; RRID: AB_10375175 (1:1000)
Anti-NDUFA10, Thermo Fisher Scientific, Cat#PA5-21474; RRID: AB_11154197 (1:1000)
Anti-COX6B1, Proteintech, Cat#11425-1-AP; RRID: AB_2085449 (1:1000)
Anti-Nur77, Thermo Fisher Scientific, Cat#14-5965-82; RRID: AB_1257215 (1:500)
Anti-NR4A2, BioLegend, Cat#682002; RRID: AB_2566567 (1:500)
Anti-ND4, Santa Cruz Biotechnology, Cat#sc-20499-R (1:1000)
Anti-CYB5B, Proteintech, Cat#15469-1-AP; RRID: AB_2230349 (1:1000)
Anti-ATP6V1D, Proteintech, Cat#14920-1-AP; RRID: AB_2243302 (1:1000)
Anti-CYTB, Proteintech, Cat# 55090-1-AP: RRID:AB_2881266 (1:1000)
Anti-alpha-Tubulin, Cell Signaling Technology, Cat# 2125; RRID:AB_2619646 (1:10000)
Anti-beta-Actin, Sigma-Aldrich, Cat# A1978; RRID:AB_476692 (1:10000)
Anti-GAPDH, Proteintech, Cat#60004-1-Ig; RRID: AB_2107436 (1:10000)

Validation

All antibodies for the species and application are validated by the manufacturers. Validation statements are on the manufacturer's websites.
Anti-α-Tubulin (Proteintech, Cat#66031-1-Ig, RRID: AB_11042766), validated in PMID: 36593399.
Anti-α-Actin-HRP (Santa Cruz Biotechnology, Cat#sc-47778, RRID: AB_2714189), validated in PMID: 8918942.
Anti-CD4 (BioLegend, Cat#100414, RRID: AB_312699), validated in PMID: 6415170.
Anti-CD8 (BioLegend, Cat#100712, RRID: AB_312751), validated in PMID: 29026144.

Anti-CD45.2 (BioLegend, Cat#109806, RRID: AB_313443), validated in PMID: 26169940.
Anti-PD-1 (BioLegend, Cat#135231, RRID: AB_2566158), validated in PMID: 20453843.
Anti-TIM-3 (BioLegend, Cat#119721, RRID: AB_2616907), validated in PMID: 34534439.
Anti-Ly108 (BioLegend, Cat#134608, RRID: AB_2188093), validated in PMID: 22683125.
Anti-CX3CR1 (BioLegend, Cat#149035, RRID: AB_2629605), validated in PMID: 37033927.
Anti-CD39 (eBioscience, Cat#25-0391-82, RRID: AB_1210502), validated in PMID: 28607488.
Anti-TIGIT (eBioscience, Cat#12-9501-80, RRID: AB_2866364), validated in PMID: 34758311.
Anti-CD69 (BioLegend, Cat#104522, RRID: AB_2260065), validated in PMID: 25135834.
Anti-GAPDH (Proteintech, Cat#60004-1-Ig, RRID: AB_2107436), validated in PMID: 36477534.
Anti-Granzyme B (BioLegend, Cat#372206, RRID: AB_2687030), validated in PMID: 33910046.
Anti-IFN-γ (BioLegend, Cat#505808, RRID: AB_315402), validated in PMID: 29120746.
Anti-LARP4 (Proteintech, Cat#16529-1-AP, RRID: AB_2296671), validated in PMID: 37169020.
Anti-NDUFB8 (Proteintech, Cat#14794-1-AP, RRID: AB_2150970), validated in PMID: 35173176.
Anti-SDHB (Proteintech, Cat#10620-1-AP, RRID: AB_2285522), validated in PMID: 34103526.
Anti-UQCRC2 (Abclonal, Cat#A4181#, RRID: AB_2765543), validated in PMID: 38834564.
Anti-ATP5A1 (Abclonal, Cat#A5884#, RRID: AB_2766632), validated in PMID: 31937931.
Anti-ND5 (Abclonal, Cat#A12465, RRID: AB_2759309), validated in PMID: 39380483.
Anti-ATP6 (Abclonal, Cat#A8193, RRID: AB_2768510), validated in PMID: 37946697.
HRP-conjugated goat anti-rat IgG (Santa Cruz Biotechnology, Cat#sc-2032, RRID: AB_631755) validated in PMID: 16467204
Anti-UQCRC1 (Thermo Fisher Scientific, Cat#459140, RRID:AB_10375175) validated in PMID: 27626371
Anti-COX6B1 (Proteintech, Cat#11425-1-AP, RRID:AB_2085449) validated in PMID: 20870728
Anti-Nur77 (Thermo Fisher Scientific, Cat#14-5965-82, RRID:AB_1257215) validated in PMID: 22996661
Anti-NR4A2 (BioLegend, Cat#682002, RRID:AB_2566567) validated in PMID: 21468021
Anti-ND4 (Santa Cruz Biotechnology, Cat#sc-20499-R) validated in PMID: 30541130
Anti-CYB5B (Proteintech, Cat#15469-1-AP, RRID:AB_2230349) validated in PMID: 32857985
Anti-ATP6V1D (Proteintech Cat# 14920-1-AP, RRID:AB_2243302) validated in PMID: 33340069
Anti-HA-probe (Y-11), Santa Cruz Biotechnology, Cat# sc-805; RRID: AB_631618, validated in PMID: 10220376

Eukaryotic cell lines

Policy information about cell lines and Sex and Gender in Research

Cell line source(s)	B16-OVA,LLC,293T and MC38 cell lines were all purchased from ATCC. Platinum-E cells were a kind gift from Qi's laboratory at Tsinghua University.
Authentication	The cell lines used in this study were not authenticated by external services.
Mycoplasma contamination	All cell lines used in this study were tested for mycoplasma contamination, and the results confirmed that they were negative for mycoplasma contamination.
Commonly misidentified lines (See ICLAC register)	No commonly misidentified cell lines listed in the ICLAC database were used in this study.

Animals and other research organisms

Policy information about studies involving animals; ARRIVE guidelines recommended for reporting animal research, and Sex and Gender in Research

Laboratory animals	Specific-pathogen-free (SPF) C57BL/6 (B6) mice were obtained from Charles River Laboratories. All experimental procedures involving mice were conducted in compliance with the guidelines of the Tsinghua University Animal Ethics Committee. B6N.129-Rpl22tm1.1Psam/J (RiboTag) mice were purchased from The Jackson Laboratory (JAX: 011029) and bred with CD4-Cre recombinase-expressing mice to generate double-homozygous animals for RPLace-seq experiments (Sanz et al., 2009). B6N.129(Cg)-Gt(ROSA)26Sortm1.1(CAG-cas9,-EGFP)Fezh/J (Cas9+) mice (JAX: 026430) were bred in-house. OT-I mice (JAX: 003831) were crossed with Cas9+ mice and subsequently maintained in-house. Female mice aged 8 to 12 weeks were used for experiments. Tumor xenograft studies were conducted using NCG (NOD/ShiLtJGpt-Prkdcem26Cd52Il2rgem26Cd22/Gpt) mice, aged 8 to 10 weeks, sourced from Gempharmatech Co., Ltd. All mice were housed under specific-pathogen-free (SPF) conditions and handled in strict accordance with the Tsinghua University Animal Ethics Committee guidelines.
Wild animals	This study did not involve wild animals.
Reporting on sex	Both male and female mice were used for the study. No differences were observed between male and female mice used in this study.
Field-collected samples	This study did not involve field-collected samples.
Ethics oversight	All mice were used in accordance with Tsinghua University Institutional Animal Care and Use Committee (IACUC) guidelines. All experiments involving human samples were approved by the Ethics Committee of Beijing Institute of Genomics, Chinese Academy of Sciences (2020S012).

Note that full information on the approval of the study protocol must also be provided in the manuscript.

Plants

Seed stocks	N/A
Novel plant genotypes	N/A
Authentication	N/A

Flow Cytometry

Plots

Confirm that:

☒ The axis labels state the marker and fluorochrome used (e.g. CD4-FITC).

☒ The axis scales are clearly visible. Include numbers along axes only for bottom left plot of group (a 'group' is an analysis of identical markers).

☒ All plots are contour plots with outliers or pseudocolor plots.

☒ A numerical value for number of cells or percentage (with statistics) is provided.

Methodology

Sample preparation	Cells were initially resuspended in FACS buffer, followed by resuspension in staining buffer and incubation with Fc Block (clone 2.4G2; BioX Cell) for 10 minutes. Subsequently, the cells were stained with the following antibodies on ice for 30 minutes: anti-CD8, anti-CD45.1, anti-CD45.2, anti-PD-1, anti-TIM-3, anti-CD69, anti-Ly108, anti-CX3CR1, anti-CD39, and anti-TIGIT, all purchased from BioLegend. For intracellular staining, the cells were fixed with fixation buffer (BioLegend) on ice for 15 minutes, then washed twice with Intracellular Staining Permeabilization Wash Buffer (BioLegend). Antibodies against IFN-γ (Clone XMG1.2), TNF-α (Clone MP6-XT22), IL-2 (Clone JES6-5H4), COX4 (Clone 3E11), and COX1 (Clone 1D6E1A8) were added and incubated for 1 hour on ice. Cytokine-producing cells and protein expression levels were determined by flow cytometry. Staining for transcription factors TOX and TCF1 was performed using the Foxp3/Transcription Factor Staining Buffer Set (Invitrogen) according to the manufacturer's instructions. Flow cytometry data were collected using a Fortessa (BD) instrument and analyzed with FlowJo software (Tree Star).
Instrument	BD LSR Fortessa
Software	FACSDiva (v8.0) was used for data acquisition. FlowJo 10.0 was used for data analysis.
Cell population abundance	CD8+ T-cells were identified by CD8-APC staining.
Gating strategy	The gating strategy was initially doublet exclusion using FSC-H and FSC-A, followed by viable cell identification via Zombie Live/Dead dye exclusion using SCC by Zombie-A. CD8+ T cells were then identified via CD8 expression using CD8-BUV496. Host and donor-derived cells were distinguished via CD45.1-BV650 and CD45.2-BV750. Further analysis of donor-derived CD8 + T cells was performed using PD-1-BV421 and TIM-3-BV605 to classify subsets, including early T_Ex (PD-1 hi TIM-3-), terminal TEx (PD-1 hi TIM-3+), and naive cells. For transferred T cells, The gating strategy was initially doublet exclusion using FSC-A and SSC-A, followed by viable cell identification via Zombie-BV570 Live/Dead dye exclusion using SSC-A. CD8+ T cells were then identified via CD8 expression using CD8-BUV737. GFP-positive sgRNA+ cells were gated to isolate genetically modified cells. Further analysis of CD8+ GFP-positive cells was performed using PD-1-BV711 and TIM-3-PE-Cy7 to classify T cell subsets, including TEX (PD-1hi TIM-3+). CX3CR1-BV510 and PD-1-BV711 expression were then used to identify effector-like T cells (TEFF-like).

☒ Tick this box to confirm that a figure exemplifying the gating strategy is provided in the Supplementary Information.